Dark Energy Survey Year 3 results: Cosmology with moments of weak lensing mass maps

M. Gatti,[1,*] B. Jain,[1] C. Chang,[2,3] M. Raveri,[1] D. Zürcher,[4] L. Secco,[1,3] L. Whiteway,[5] N. Jeffrey,[5,6] C. Doux,[1] T. Kacprzak,[4] D. Bacon,[7] P. Fosalba,[8,9] A. Alarcon,[10] A. Amon,[11] K. Bechtol,[12] M. Becker,[10] G. Bernstein,[13] J. Blazek,[14,15] A. Campos,[16] A. Choi,[17] C. Davis,[18] J. Derose,[19] S. Dodelson,[20,21] F. Elsner,[5] J. Elvin-Poole,[22,23] S. Everett,[24] A. Ferte,[25] D. Gruen,[26] I. Harrison,[27,28] D. Huterer,[29] M. Jarvis,[1] E. Krause,[30] P. F. Leget,[10] P. Lemos,[5,31] N. Maccrann,[32] J. Mccullough,[18] J. Muir,[33] J. Myles,[34,18,35] A. Navarro,[35] S. Pandey,[1] J. Prat,[2,3] R. P. Rollins,[27] A. Roodman,[10,35] C. Sanchez,[1] E. Sheldon,[36] T. Shin,[1] M. Troxel,[37] I. Tutusaus,[38,39] B. Yin,[20] M. Aguena,[40] S. Allam,[41] F. Andrade-Oliveira,[40,42] J. Annis,[41] E. Bertin,[43,44] D. Brooks,[5] D. L. Burke,[18,35] A. Carnero Rosell,[40] M. Carrasco Kind,[45,46] J. Carretero,[47] R. Cawthon,[12] M. Costanzi,[48,49,50] L. N. da Costa,[40,51] M. E. S. Pereira,[29,52] J. De Vicente,[53] S. Desai,[54] H. T. Diehl,[41] J. P. Dietrich,[26] P. Doel,[5] A. Drlica-Wagner,[2,3,41] K. Eckert,[1] A. E. Evrard,[29,55] I. Ferrero,[56] J. García-Bellido,[57] E. Gaztanaga,[8,9] T. Giannantonio,[58,59] R. A. Gruendl,[45,46] J. Gschwend,[60,51] G. Gutierrez,[41] S. R. Hinton,[61] D. L. Hollowood,[24] K. Honscheid,[22,23] D. J. James,[62] K. Kuehn,[63,64] N. Kuropatkin,[41] O. Lahav,[5] C. Lidman,[65,66] M. A. G. Maia,[60,51] J. L. Marshall,[67] P. Melchior,[68] F. Menanteau,[45,46] R. Miquel,[47,69] R. Morgan,[12] A. Palmese,[70] F. Paz-Chinchón,[45,58] A. Pieres,[40,51] A. A. Plazas Malagón,[68] K. Reil,[35] M. Rodriguez-Monroyv,[53] A. K. Romer,[31] E. Sanchez,[53] M. Schubnell,[29] S. Serrano,[38,9] I. Sevilla-Noarbe,[53] M. Smith,[71] M. Soares-Santos,[29] E. Suchyta,[72] G. Tarle,[29] D. Thomas,[7] C. To,[34,18,35] and T. N. Varga[73,74]

(DES Collaboration)

[1]*Department of Physics and Astronomy, University of Pennsylvania, Philadelphia, Pennsylvania 19104, USA*
[2]*Department of Astronomy and Astrophysics, University of Chicago, Chicago, Illinois 60637, USA*
[3]*Kavli Institute for Cosmological Physics, University of Chicago, Chicago, Illinois 60637, USA*
[4]*Department of Physics, ETH Zurich, Wolfgang-Pauli-Strasse 16, CH-8093 Zurich, Switzerland*
[5]*Department of Physics and Astronomy, University College London, Gower Street, London WC1E 6BT, United Kingdom*
[6]*Laboratoire de Physique de l'Ecole Normale Supérieure, ENS, Université PSL, CNRS, Sorbonne Université, Université de Paris, Paris 75005, France*
[7]*Institute of Cosmology and Gravitation, University of Portsmouth, Portsmouth PO1 3FX, United Kingdom*
[8]*Institut d'Estudis Espacials de Catalunya (IEEC), 08034 Barcelona, Spain*
[9]*Institute of Space Sciences (ICE, CSIC), Campus UAB, Carrer de Can Magrans, s/n, 08193 Barcelona, Spain*
[10]*Argonne National Laboratory, 9700 South Cass Avenue, Lemont, Illinois 60439, USA*
[11]*Kavli Institute for Particle Astrophysics and Cosmology, P. O. Box 2450, Stanford University, Stanford, California 94305, USA*
[12]*Physics Department, 2320 Chamberlin Hall, University of Wisconsin-Madison, 1150 University Avenue Madison, Wisconsin 53706-1390, USA*
[13]*Department of Physics and Astronomy, University of Pennsylvania, Philadelphia, Pennsylvania 19104, USA*
[14]*Department of Physics, Northeastern University, Boston, Massachusetts 02115, USA*
[15]*Laboratory of Astrophysics, École Polytechnique Fédérale de Lausanne (EPFL), Observatoire de Sauverny, 1290 Versoix, Switzerland*
[16]*Department of Physics, Carnegie Mellon University, Pittsburgh, Pennsylvania 15312, USA*
[17]*California Institute of Technology, 1200 East California Blvd, MC 249-17, Pasadena, California 91125, USA*
[18]*Kavli Institute for Particle Astrophysics and Cosmology, P. O. Box 2450, Stanford University, Stanford, California 94305, USA*
[19]*Lawrence Berkeley National Laboratory, 1 Cyclotron Road, Berkeley, California 94720, USA*
[20]*Department of Physics, Carnegie Mellon University, Pittsburgh, Pennsylvania 15312, USA*
[21]*NSF AI Planning Institute for Physics of the Future, Carnegie Mellon University, Pittsburgh, Pennsylvania 15213, USA*
[22]*Center for Cosmology and Astro-Particle Physics, The Ohio State University, Columbus, Ohio 43210, USA*

[23]*Department of Physics, The Ohio State University, Columbus, Ohio 43210, USA*
[24]*Santa Cruz Institute for Particle Physics, Santa Cruz, California 95064, USA*
[25]*Jet Propulsion Laboratory, California Institute of Technology, 4800 Oak Grove Dr., Pasadena, California 91109, USA*
[26]*Faculty of Physics, Ludwig-Maximilians-Universität, Scheinerstr. 1, 81679 Munich, Germany*
[27]*Department of Physics, University of Oxford, Denys Wilkinson Building, Keble Road, Oxford OX1 3RH, United Kingdom*
[28]*Jodrell Bank Center for Astrophysics, School of Physics and Astronomy, University of Manchester, Oxford Road, Manchester M13 9PL, United Kingdom*
[29]*Department of Physics, University of Michigan, Ann Arbor, Michigan 48109, USA*
[30]*Department of Astronomy/Steward Observatory, University of Arizona, 933 North Cherry Avenue, Tucson, Arizona 85721-0065, USA*
[31]*Department of Physics and Astronomy, Pevensey Building, University of Sussex, Brighton BN1 9QH, United Kingdom*
[32]*Department of Applied Mathematics and Theoretical Physics, University of Cambridge, Cambridge CB3 0WA, United Kingdom*
[33]*Perimeter Institute for Theoretical Physics, 31 Caroline St. North, Waterloo, Ontario N2L 2Y5, Canada*
[34]*Department of Physics, Stanford University, 382 Via Pueblo Mall, Stanford, California 94305, USA*
[35]*SLAC National Accelerator Laboratory, Menlo Park, California 94025, USA*
[36]*Brookhaven National Laboratory, Bldg 510, Upton, New York 11973, USA*
[37]*Department of Physics, Duke University Durham, North Carolina 27708, USA*
[38]*Institut d'Estudis Espacials de Catalunya (IEEC), 08034 Barcelona, Spain*
[39]*Institute of Space Sciences (ICE, CSIC), Campus UAB, Carrer de Can Magrans, s/n, 08193 Barcelona, Spain*
[40]*Laboratório Interinstitucional de e-Astronomia—LIneA, Rua Gal. José Cristino 77, Rio de Janeiro RJ-20921-400, Brazil*
[41]*Fermi National Accelerator Laboratory, P. O. Box 500, Batavia, Illinois 60510, USA*
[42]*Instituto de Física Teórica, Universidade Estadual Paulista, São Paulo 01140-070, Brazil*
[43]*CNRS, UMR 7095, Institut d'Astrophysique de Paris, F-75014 Paris, France*
[44]*Sorbonne Universités, UPMC Univ Paris 06, UMR 7095, Institut d'Astrophysique de Paris, F-75014 Paris, France*
[45]*Center for Astrophysical Surveys, National Center for Supercomputing Applications, 1205 West Clark St., Urbana, Illinois 61801, USA*
[46]*Department of Astronomy, University of Illinois at Urbana-Champaign, 1002 W. Green Street, Urbana, Illinois 61801, USA*
[47]*Institut de Física d'Altes Energies (IFAE), The Barcelona Institute of Science and Technology, Campus UAB, 08193 Bellaterra, Barcelona, Spain*
[48]*Astronomy Unit, Department of Physics, University of Trieste, via Tiepolo 11, I-34131 Trieste, Italy*
[49]*INAF-Osservatorio Astronomico di Trieste, via G. B. Tiepolo 11, I-34143 Trieste, Italy*
[50]*Institute for Fundamental Physics of the Universe, Via Beirut 2, 34014 Trieste, Italy*
[51]*Observatório Nacional, Rua Gal. José Cristino 77, Rio de Janeiro RJ-20921-400, Brazil*
[52]*Hamburger Sternwarte, Universität Hamburg, Gojenbergsweg 112, 21029 Hamburg, Germany*
[53]*Centro de Investigaciones Energéticas, Medioambientales y Tecnológicas (CIEMAT), Madrid 28040, Spain*
[54]*Department of Physics, IIT Hyderabad, Kandi, Telangana 502285, India*
[55]*Department of Astronomy, University of Michigan, Ann Arbor, Michigan 48109, USA*
[56]*Institute of Theoretical Astrophysics, University of Oslo. P.O. Box 1029 Blindern, NO-0315 Oslo, Norway*
[57]*Instituto de Fisica Teorica UAM/CSIC, Universidad Autonoma de Madrid, 28049 Madrid, Spain*
[58]*Institute of Astronomy, University of Cambridge, Madingley Road, Cambridge CB3 0HA, United Kingdom*
[59]*Kavli Institute for Cosmology, University of Cambridge, Madingley Road, Cambridge CB3 0HA, United Kingdom*
[60]*Laboratório Interinstitucional de e-Astronomia—LIneA, Rua Gal. José Cristino 77, Rio de Janeiro, RJ-20921-400, Brazil*
[61]*School of Mathematics and Physics, University of Queensland, Brisbane, Queensland 4072, Australia*
[62]*Center for Astrophysics | Harvard & Smithsonian, 60 Garden Street, Cambridge, Massachusetts 02138, USA*
[63]*Australian Astronomical Optics, Macquarie University, North Ryde, New South Wales 2113, Australia*
[64]*Lowell Observatory, 1400 Mars Hill Rd, Flagstaff, Arizona 86001, USA*

[65]Centre for Gravitational Astrophysics, College of Science, The Australian National University, Australian Capital Territory 2601, Australia
[66]The Research School of Astronomy and Astrophysics, Australian National University, Australian Capital Territory 2601, Australia
[67]George P. and Cynthia Woods Mitchell Institute for Fundamental Physics and Astronomy, and Department of Physics and Astronomy, Texas A&M University, College Station, Texas 77843, USA
[68]Department of Astrophysical Sciences, Princeton University, Peyton Hall, Princeton, New Jersey 08544, USA
[69]Institució Catalana de Recerca i Estudis Avançats, E-08010 Barcelona, Spain
[70]Department of Astronomy, University of California, Berkeley, 501 Campbell Hall, Berkeley, California 94720, USA
[71]School of Physics and Astronomy, University of Southampton, Southampton SO17 1BJ, United Kingdom
[72]Computer Science and Mathematics Division, Oak Ridge National Laboratory, Oak Ridge, Tennessee 37831, USA
[73]Max Planck Institute for Extraterrestrial Physics, Giessenbachstrasse, 85748 Garching, Germany
[74]Universitäts-Sternwarte, Fakultät für Physik, Ludwig-Maximilians Universität München, Scheinerstr. 1, 81679 München, Germany

(Received 13 November 2021; accepted 30 August 2022; published 12 October 2022)

We present a cosmological analysis using the second and third moments of the weak lensing mass (convergence) maps from the first three years of data (Y3) data of the Dark Energy Survey. The survey spans an effective area of 4139 square degrees and uses the images of over 100 million galaxies to reconstruct the convergence field. The second moment of the convergence as a function of smoothing scale contains information similar to standard shear 2-point statistics. The third moment, or the skewness, contains additional non-Gaussian information. The data is analyzed in the context of the ΛCDM model, varying five cosmological parameters and 19 nuisance parameters modeling astrophysical and measurement systematics. Our modeling of the observables is completely analytical, and has been tested with simulations in our previous methodology study. We obtain a 1.7% measurement of the amplitude of fluctuations parameter $S_8 \equiv \sigma_8(\Omega_m/0.3)^{0.5} = 0.784 \pm 0.013$. The measurements are shown to be internally consistent across redshift bins, angular scales, and between second and third moments. In particular, the measured third moment is consistent with the expectation of gravitational clustering under the ΛCDM model. The addition of the third moment improves the constraints on S_8 and Ω_m by ∼15% and ∼25% compared to an analysis that only uses second moments. We compare our results with *Planck* constraints from the cosmic microwave background, finding a 2.2–2.8σ tension in the full parameter space, depending on the combination of moments considered. The third moment, independently, is in 2.8σ tension with *Planck*, and thus provides a cross-check on the analyses of 2-point correlations.

DOI: 10.1103/PhysRevD.106.083509

I. INTRODUCTION

Gravitational lensing is one of the cleanest probes for studying the mass distribution in the Universe. General relativity predicts that the trajectories of photons emitted by distant galaxies are bent as they pass through regions of space-time perturbed by the mass distribution between the galaxy and the observer [1]. When studying the light emitted by distant galaxies, the level of distortion induced by the mass distribution of the Universe, or large scale structure (LSS), is usually small, at the percent level—the regime of weak gravitational lensing. By collecting observations and measuring the shapes of many galaxies, statistical tools can be used to infer the mass distribution of the Universe [2–8]. Ongoing and future surveys (DES, Dark Energy Survey Collaboration [9]; Kilo-Degree Survey KIDS, Kuijken *et al.* [10]; Hyper Suprime-Cam HSC, Aihara *et al.* [11]; *Vera C. Rubin Observatory's Legacy Survey*, LSST Science Collaboration *et al.* [12]; Euclid, Laureijs *et al.* [13]) are currently measuring (or planning to measure) the shapes of tens to hundreds of millions of galaxies, spanning thousands of square degrees of the sky. In particular, DES recently measured 100 million galaxies spanning ∼5000 square degrees of the southern hemisphere [14], and created the largest map of the mass distribution of the Universe from a galaxy survey [4].

For a given cosmological model, the statistical properties of the mass distribution can be predicted over time. Second-order statistics, such as correlation functions [15–19], the power spectrum [20], or the waveletlike COSEBIs

*marcogatti29@gmail.com

(complete orthogonal sets of E/B integrals) [21], are standard tools used to exploit the Gaussian information of the mass maps. However, a weak lensing mass map contains information beyond that captured by second-order statistics, as its probability distribution function (PDF) has non-Gaussian features induced by gravitational evolution. In particular, the PDF of the mass distribution in the late Universe is roughly approximated by a log-normal [22–24], a fact that has also been investigated for the weak lensing convergence field with DES data [25].

Higher-order statistics are appealing, as their use can improve constraints on cosmological parameters [26–29] over standard 2-point statistics, or can help discriminate between extended models such as modified gravity theories [30,31]. Numerous tools have been developed to extract the non-Gaussian information from mass maps. Higher-order statistics commonly used with weak lensing include shear peak statistics [5,29,31–37], higher moments of the weak lensing convergence field [2,7,26,27,31,38,39], three-point correlation functions or bispectra [40–43], Minkowski functionals [27,44–46], and machine-learning methods [47–50]. Many of these have recently been applied to data [5,34,36,47,49], often performing well in terms of cosmological constraints. The theoretical modeling of some of these statistics is often complex, and large suites of N-body simulations, spanning the parameter space considered in the analysis, are used to model the observables.

This work focuses on the use of second and third moments of weak lensing mass maps to constrain cosmology. Moments have been studied in the past, and have been measured both in data and simulations [2,7,27,28,51–54], although they have not been used to place constraints on cosmological parameters. Tests using simulations have shown improvements to cosmological constraints arising from using moments of order higher than second [26–28]. The methodology used in this paper has been developed and tested using simulations in a companion paper, [26] (hereafter G20). Although the methodology can be applied to any dataset, the analysis in G20 was geared towards the first three years of data of DES. The modeling of second and third moments developed in G20 is based on theoretical predictions, therefore it does not rely on large suites of N-body simulations (though the predictions are tested against simulations); moreover, observational systematics errors such as photometric redshift uncertainties or intrinsic alignment are modeled and marginalized during the analysis. This work applies that methodology to the first three years of data (Y3) from DES, presenting the cosmological constraints, discussing a number of observational systematic null tests, and comparing the results with constraints from other DES Y3 probes and/or external datasets (e.g., *Planck*).

The paper is organized as follows: Section II describes the data and simulations used in this work; Sec. III provides a short description of the theoretical modeling of the observables used in the analysis (the second and third moments of the convergence field); Sec. IV describes the likelihood and the covariance used in the cosmological parameter inference, and discusses the priors adopted in the analysis; Sec. V summarizes the preunblinding tests; Sec. VI presents the cosmological results, along with a number of internal consistency tests and comparisons with results from other DES analyses or from analyses using external data sets; Sec. VII summarizes our findings.

II. DATA AND SIMULATIONS

A. Data

The main goal of our analysis is to measure second and third moments of the convergence field and use them to estimate cosmological parameters. To this aim, we use the weak lensing catalog from the first three years (Y3) of the DES [14].

DES [9] is a six-year survey that spans ∼5000 deg^2 of the southern hemisphere. Images have been taken in *grizY* filters by the 570 megapixel Dark Energy Camera [DECam, [55]], mounted on the Cerro Tololo Inter-American Observatory (CTIO) four-meter Blanco telescope in Chile. The raw images were processed by the DES Data Management (DESDM) team [56–58]. Full details about the image processing are provided in [56,57].

The DES Y3 weak lensing sample is described in detail in [14] and builds upon the Y3 Gold catalog [59]. It is created using the METACALIBRATION algorithm [60,61], which infers the galaxy ellipticities starting from noisy images of the detected objects in the r, i, z bands. The METACALIBRATION algorithm was used previously in the DES Y1 analysis [62]. METACALIBRATION uses an approximate estimator of the shear field and self-calibrates it using the response of the estimator to shear as well as to selection effects. A number of selection cuts are designed to remove objects in the catalog potentially affected by systematic effects [14]. An inverse variance weight is also assigned to galaxies in order to enhance the overall signal-to-noise. The final DES Y3 shear catalog has 100,204,026 objects, with a weighted $n_{\rm eff} = 5.59$ galaxies arcmin^{-2}, over an effective area of 4139 square degrees.

Although the METACALIBRATION self-calibration procedure removes most of the multiplicative bias, for the DES Y3 weak lensing sample there is a known residual additional multiplicative bias at the level of 2 or 3 per cent [63]. This residual bias stems mostly from a shear-redshift-dependent detection bias due to blending of galaxy images, for which the METACALIBRATION implementation adopted in DES Y3 is unable to account [64]. We do not calibrate for this factor at the catalog level, but we do marginalize over it in the analysis. In [14] the weak lensing sample has also been tested for additive biases (e.g., due to point-spread-function residuals). In particular, the catalog is characterized by a nonzero mean shear whose origin is

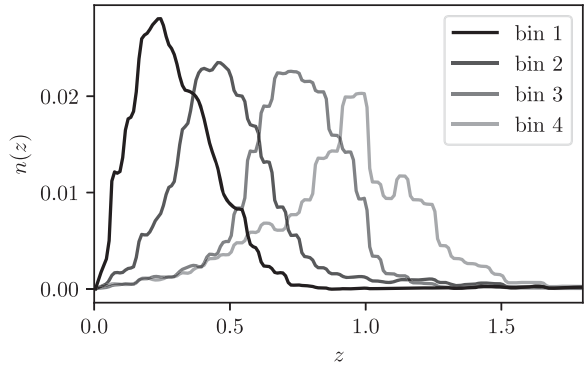

FIG. 1. Redshift distributions as estimated in data for the four DES Y3 tomographic bins [65].

unknown and which is subtracted at the catalog level before performing any analysis.

The weak lensing sample is divided into four tomographic bins of roughly equal number density using the SOMPZ method [65]; SOMPZ, in combination with constraints from clustering redshifts [66], also provides redshift distribution estimates (see Fig. 1). The $n(z)$'s are further tweaked to take into account the redshift-dependent effects of blending [63]. During the cosmological analysis, additional constraints on the redshift distributions are provided by shear ratios [67]. Shear ratios are ratios of small-scale galaxy-galaxy lensing measurements obtained using different source samples (in this case, different weak lensing tomographic bins) and a common lens sample. Not only do they improve constraints on redshift distributions, but they also help constraining both intrinsic alignment parameters and cosmological parameters.

A two-stage blinding scheme was implemented for all DES Y3 cosmological analyses in order to avoid intentional or unintentional confirmation bias. First, the weak lensing sample was blinded by means of a multiplicative factor, in a fashion similar to what was adopted in the Y1 analysis [62]. In particular, the ellipticities $\mathbf{e}$ of the catalog were transformed via $|\boldsymbol{\eta}| \equiv 2\mathrm{arctanh}|\mathbf{e}| \to f|\boldsymbol{\eta}|$, with a hidden value $0.9 < f < 1.1$. After all the catalog and map-based systematic tests were passed [4,14], the hidden value was revealed and the catalog unblinded. This work ignores this first level of blinding, as when we started analysing the DES Y3 data the catalog had already been validated and unblinded. The second level of blinding, which follows the work of [68], was applied to the summary statistics under examination; in this case, it was applied to the measured second and third moments of the convergence field. In particular, to each element $\hat{d}_i$ of the observable vector (i.e., both second and third moments), the following transformation was applied,

$$\hat{d}_i^{\mathrm{blinded}} = \hat{d}_i + d_i(\Theta_{\mathrm{ref}} + \Delta\Theta) - d_i(\Theta_{\mathrm{ref}}). \quad (1)$$

In the above equation, d_i is a theory data vector computed at a given cosmology Θ; Θ_{ref} is a fiducial cosmology (we used the DES Y1 3 × 2pt cosmology from [69]), and $\Delta\Theta$ is a blind shift in the cosmological parameters (drawn from a distribution three times larger than the DES Y1 3 × 2pt posterior).

A number of systematic tests were performed on blinded data vectors (see Sec. V) before proceeding to inspect the unblinded cosmological results.

B. Simulations

Covariance matrices for our measurement are generated: (a) for our fiducial covariance, using log-normal realizations from FLASK [70], (b) for testing, using the N-body simulation hereafter called "T17" [71], and (c) also for testing, using the N-body simulation PKDGRAV [72]. Moreover, both T17 and PKDGRAV simulations are used to validate our modeling (Appendix B). Such a validation was already performed in G20, but using only T17 simulations; we repeat that here, for both sets of N-body simulations, with updated analysis choices.

1. FLASK realizations

We use the FLASK (Full-sky Lognormal Astro-fields Simulation Kit) software [70] to rapidly generate full-sky, log-normal realizations of the convergence field. FLASK assumes the convergence field to be described by a zero-mean shifted log-normal distribution, where the parameters of the log-normal probability distribution function (PDF) are chosen to match the variance and skewness of the input. We use here the 1000 independent FLASK realizations produced for the validation of the DES Y3 3 × 2pt covariance [73]. The lognormal approximation for the covariance has been shown to be sufficient to not bias the recovery of the cosmological parameters in G20. The cosmological parameters of the input power spectra used for the FLASK realizations are $\Omega_{\mathrm{m}} = 0.3$, $\sigma_8 = 0.82355$, $\Omega_{\mathrm{b}} = 0.048$, $n_{\mathrm{s}} = 0.97$, $h_{100} = 0.69$ and $\Omega_\nu h = 0.00083$. We also assumed DES Y3 redshift distributions. The FLASK convergence realizations were provided in maps using the Hierarchical Equal Area isoLatitude Pixelation scheme (HEALPIX, [74]) with resolution NSIDE $= 4096$. In order to create a simulated weak lensing galaxy catalog, we then used the position, shape noise (obtained by randomly rotating each galaxy), and weight of the galaxies of the fiducial DES Y3 weak lensing catalog; depending on the position of each individual galaxy, we sampled the simulated shear maps and added shape noise accordingly. This procedure allows us to generate 1000 independent simulated shear catalogs.

2. T17 simulations

The first set of N-body simulations used in this work are the T17 [71] simulations. The set consists of 108 full-sky lensing convergence and shear maps, spanning a wide redshift range (between $z = 0.05$ and 5.3) at intervals of 150 h^{-1} Mpc comoving distance. The N-body simulations

assume a WMAP 9 cosmology ($\Omega_m = 0.279$, $\sigma_8 = 0.82$, $\Omega_b = 0.046$, $n_s = 0.97$, $h = 0.7$), and were run using L-GADGET2 [75]. Initial conditions were generated using 2LPTIC [76].

The simulations begin with 14 boxes in steps of 450 h^{-1} Mpc, with total side lengths of L = 450, 900, 1350, …, 6300 h^{-1} Mpc. There are six independent copies at each box size and 2048^3 particles per box. Lens plane snapshots are taken at intervals of 150 h^{-1} Mpc comoving distance. The expected accuracy of the average matter power spectra from the simulations (compared to predictions from the revised HALOFIT, [77]) is within 5% for $k < 1$ h Mpc^{-1} at $z < 1$, for $k < 0.8$ h Mpc^{-1} at $z < 3$, and for $k < 0.5$ h Mpc^{-1} at $z < 7$ [71]. Weak lensing quantities for each simulation were estimated using the multiple plane ray-tracing algorithm GRAYTRIX [78], and shear and convergence HEALPIX maps with resolution NSIDE = 4096 are provided.

For each of the 108 simulations, we cut out four independent (i.e., nonoverlapping) regions corresponding to the DES Y3 footprint. We then stacked the convergence and shear snapshots at different redshift to produce convergence and shear maps for the four weak lensing tomographic bins. This gave us 432 independent realizations of the shear field for each tomographic bin. In order to create a simulated weak lensing galaxy catalog, we used the position, shape noise (obtained by randomly rotating each galaxy), and weight of the galaxies of the fiducial DES Y3 weak lensing catalog; depending on the position of each individual galaxy, we sampled the simulated shear maps and added shape noise accordingly. We ended up with 432 independent simulated shear catalogs from T17 simulations.

3. PKDGRAV simulations

The second set of N-body simulations is the DarkGridV1 suite, produced using the PKDGRAV3 code [72] and described in detail in [29,79]. In particular, we use 50 independent realizations at the fixed cosmology $\Omega_m = 0.26$, $\sigma_8 = 0.84$, $\Omega_b = 0.0493$, $n_s = 0.9649$, $h = 0.673$. All simulations include three massive neutrino species with a mass of $m_\nu = 0.02$ eV per species [79]. The simulations were obtained using 14 replicated boxes in each direction (14^3 replicas in total) so as to span the redshift interval between z = 0 and z = 3. Each individual box contains 768^3 particles and has a side length of 900 h^{-1} Mpc. Such a configuration is known to yield a field variance that is too small at very large scales [47]; however, such scales are not considered in this work. For each simulation, lens planes are provided at ∼87 redshifts between $z = 3.0$ and $z = 0.0$, equally spaced in proper time. Lensing quantities (shear and convergence) were obtained under the Born approximation. For each simulation, we cut out four independent DES Y3 footprints and thereby created 200 independent catalogs in a fashion similar to the T17 simulations.

III. THEORETICAL MODELING

We provide here a short summary of the theoretical modeling of our observables. Further details are provided in G20.

Our cosmological analysis relies on the theoretical modeling of the second and third moments of convergence maps, which is based on cosmological perturbation theory [80–82]. Consider three convergence maps, obtained from different tomographic bins (labeled i, j, k) of the weak lensing catalog (the equations below apply for more tomographic bins as well, taken two or three at a time). The maps are smoothed by a top-hat filter of smoothing length θ_0. The second and third moments are then given by

$$\langle\kappa^2_{\theta_0}\rangle^{i,j,\mathrm{EE/BB}} = \int d\chi \frac{q^i(\chi)q^j(\chi)}{\chi^2} \times \sum_\ell \frac{2\ell+1}{4\pi} f_\ell^{-1} W_\ell(\theta_0)^2 \times \sum_{\ell'} M^{\mathrm{EE/BB,EE}}_{\ell\ell'} P_{\mathrm{NL}}(\ell'/\chi,\chi) F^2_{\ell'} f_{\ell'}, \quad (2)$$

$$\langle\kappa^3_{\theta_0}\rangle^{i,j,k,\mathrm{EE/BB}} = \int d\chi \frac{q^i(\chi)q^j(\chi)q^k(\chi)}{\chi^4} \times S_3\left[\sum_\ell \frac{2\ell+1}{4\pi} f_\ell^{-1} W_\ell(\theta_0)^2 \times \sum_{\ell'} M^{\mathrm{EE/BB,EE}}_{\ell\ell'} P_{\mathrm{NL}}(\ell'/\chi,\chi) F^2_{\ell'} f_{\ell'}\right]^2. \quad (3)$$

Here the lensing kernel term q^i is given by

$$q^i(\chi) = \frac{3H_0^2\Omega_m}{2c^2}\frac{\chi}{a(\chi)}\int_\chi^{\chi_h} d\chi' n^i(z(\chi'))dz/d\chi'\frac{\chi'-\chi}{\chi}, \quad (4)$$

where χ is comoving distance, χ_h is the horizon comoving distance, H_0 the Hubble constant at the present time, c the speed of light, $n^i(z)$ the normalized redshift distribution of a given tomographic bin, and $a(\chi)$ the scale factor. Furthermore, in Eqs. (2) and (3), $W_\ell(\theta_0)$ represents the top-hat filter of smoothing length θ_0 in harmonic space, defined as

$$W_\ell(\theta_0) = \frac{P_{\ell-1}(\cos(\theta_0)) - P_{\ell+1}(\cos(\theta_0))}{(2\ell+1)(1-\cos(\theta_0))}, \quad (5)$$

where P_ℓ are Legendre polynomials of order ℓ. Other terms in Eqs. (2) and (3) are the mode-coupling matrices $M^{\mathrm{EE/BB,EE}}_{\ell\ell'}$ (e.g., [83,84], or Appendix B of G20), which take into account the effects of masking; the factor $f_\ell = [(\ell+2)(\ell-1)]/[\ell(\ell+1)]$, which accounts for the mode-coupling matrix being applied to the shear field rather than to the convergence field directly, the pixel window function F_ℓ, the nonlinear power spectrum $P_{\mathrm{NL}}(\ell/\chi,\chi)$, modeled using HALOFIT as detailed in [85], and the reduced

skewness parameter S_3. The full derivation of S_3 is provided in Appendix A of G20, where it is evaluated to leading order in perturbation theory with the addition of a small-scale refinement (in the form of analytical fitting formulas) based on N-body simulations from [81]. In G20 we determined the range (i.e., angular scales and redshift interval) of validity of our S_3 model to ensure that modeling uncertainties will not affect our cosmological analysis. Since G20, however, some of our analysis choices changed; in particular, we updated the redshift distributions, the catalog shape noise, the measurement covariance, and the nuisance parameters priors, to reflect the updates in the DES Y3 data and modeling. Moreover, we include galaxy-galaxy lensing information from small scales in the form of shear ratios. Therefore, we repeated the modeling validation performed in G20 in Appendix B, using our updated analysis choices. Moreover, we validated our modeling on two different sets of N-body simulations (T17 and PKDGRAV).

A. Systematic effects

We model astrophysical and measurement systematic effects through nuisance parameters, over which we marginalize when estimating the cosmological parameters. Here is a short description of the nuisance parameters used in this work; priors are summarized in Table I.

Photometric redshift uncertainties. The first type of nuisance parameters are "calibration" parameters that model uncertainties in the photometric redshift estimates from the SOMPZ method. Such uncertainties are parametrized through a shift Δz in the mean of the redshift distributions

$$n^i(z) = \hat{n}^i(z + \Delta z), \tag{6}$$

where $\hat{n}^i$ is the original estimate of the redshift distribution for bin i. We assume DES Y3 priors for the shift parameters. The priors also include the additional photo-z uncertainty due to blending [63]. This parametrization of the redshift uncertainties was shown to be adequate for the DES Y3 2-point analysis [15,86]; we nonetheless explore in Sec. VI a more complex parametrization of redshift uncertainties that also accounts for uncertainties in the shape of the redshift distributions.

Multiplicative shear biases. Biases coming from the shear measurement pipeline are modeled through an average multiplicative parameter $1 + m^i$ for each tomographic bin. The effect of multiplicative shear biases on the measured moments can be modeled via,

$$\langle \kappa^2_{\theta_0} \rangle^{i,j} \to (1 + m^i)(1 + m^j)\langle \kappa^2_{\theta_0} \rangle^{i,j}, \tag{7}$$

$$\langle \kappa^3_{\theta_0} \rangle^{i,j,k} \to (1 + m^i)(1 + m^j)(1 + m^k)\langle \kappa^3_{\theta_0} \rangle^{i,j,k}. \tag{8}$$

We assume Gaussian priors for each of the m^i estimated following [63].

TABLE I. Cosmological and nuisance parameters. The cosmological parameters considered are Ω_m, σ_8, Ω_b, n_s, and h. The "calibration" nuisance parameters are the multiplicative shear biases m_i and the mean photometric uncertainties of the weak lensing samples Δz_i, where the index i runs over the tomographic bins. The "astrophysical" nuisance parameters $A_{IA,0}$ and α_{IA} describe the intrinsic alignment model. The parameters Δz_i^{lens}, $\delta_{z,i}^{lens}$ and b_g^i describe the mean photometric uncertainty, the width *of* photometric uncertainty, and the galaxy matter bias of the lens sample used for the shear ratio likelihood (Sec. IV). Note that the fact that the lens mean photometric uncertainties priors are not centred at 0 is related to a different definition of the priors compared to the sources' ones. In the "Prior" column we report either lower and upper boundaries (for flat priors) or the mean and standard deviation (for Gaussian priors; note that in this case we sample over a range much broader than the one σ width). Priors are described in Sec. III A.

Parameter	Prior
Cosmological parameters	
Ω_m	$U[0.1, 0.9]$
σ_8	$U[0.5, 1.4]$
Ω_b	$U[0.03, 0.07]$
n_s	$U[0.87, 1.07]$
h	$U[0.55, 0.91]$
Calibration parameters	
m_1	$\mathcal{N}(-0.0063, 0.0091)$
m_2	$\mathcal{N}(-0.0198, 0.0078)$
m_3	$\mathcal{N}(-0.0241, 0.0076)$
m_4	$\mathcal{N}(-0.0369, 0.0076)$
Δz_1	$\mathcal{N}(0.0, 0.018)$
Δz_2	$\mathcal{N}(0.0, 0.015)$
Δz_3	$\mathcal{N}(0.0, 0.011)$
Δz_4	$\mathcal{N}(0.0, 0.017)$
Intrinsic alignment parameters	
$A_{IA,0}$	$U[-5, 5]$
α_{IA}	$U[-5, 5]$
Shear ratios parameters	
Δz_1^{lens}	$\mathcal{N}(-0.009, 0.007)$
Δz_2^{lens}	$\mathcal{N}(-0.035, 0.011)$
Δz_3^{lens}	$\mathcal{N}(-0.005, 0.006)$
$\delta_{z,1}^{lens}$	$\mathcal{N}(0.975, 0.062)$
$\delta_{z,2}^{lens}$	$\mathcal{N}(1.306, 0.093)$
$\delta_{z,3}^{lens}$	$\mathcal{N}(0.870, 0.054)$
b_g^1	$U[0, 3]$
b_g^2	$U[0, 3]$
b_g^3	$U[0, 3]$

Intrinsic galaxy alignments (IA). We model IA following the nonlinear alignment (NLA) model [87–89]. It can be included in our modeling introducing $\delta_I = A(z)\delta$, which is the density contrast responsible for the intrinsic alignment, related to the matter density contrast δ. In the NLA model, the IA amplitude can be written as a power law,

$$A(z) = -A_{IA,0}\left(\frac{1+z}{1+z_0}\right)^{\alpha_{IA}} \frac{c_1 \rho_{m,0}}{D(z)}, \tag{9}$$

with $z_0 = 0.62$, $c_1\rho_{\rm crit} = 0.0134$, with $\rho_{\rm crit} = \rho_{m,0}/\Omega_{\rm m}$ [87] and $D(z)$ the linear growth factor [90]. For second moments, the NLA model can be incorporated in our theoretical predictions by modifying the lensing kernel,

$$q^i(\chi) \to q^i(\chi) + A(z(\chi))\frac{n^i(z(\chi))}{\langle n^i\rangle}\frac{dz}{d\chi}. \tag{10}$$

For third moments, we make the assumption that the NLA contribution follows the perturbation theory relation for the actual signal. [89] have shown this is in reasonable agreement with measurements from hydrodynamical simulations, so we follow them and modify Eq. (3) as follows:

$$\begin{aligned} q^iq^jq^k \to q^iq^jq^k + \frac{A^2+2A}{3}(q^iq^jn^k + \text{cycl.}) \\ + \frac{A^2+2A^3}{3}(q^in^jn^k + \text{cycl.}) + A^4(n^in^jn^k), \end{aligned} \tag{11}$$

where in the above equation we dropped the redshift dependence for sake of simplicity; moreover, we used $n = \frac{n^i(z(\chi))}{\langle n^i\rangle}\frac{dz}{d\chi}$, and cycl. refers to the cyclic permutation of the indexes i, j, k for the terms in parenthesis. We marginalize over $A_{\rm IA,0}$ and $\alpha_{\rm IA}$ assuming flat priors. The fiducial DES Y3 3×2pt analysis adopted a different, more general model for the intrinsic galaxy alignment, called "TATT" (Tidal Alignment and Tidal Torquing; [91]), that can capture the "tidal torquing" relevant for determining the angular momentum of spiral galaxies. Tidal torquing is ignored in the NLA model, which can account only for the tidal alignment of galaxies. We did not implement such a general model here; the DES Y3 cosmic shear analysis [18] found a weak preference for simpler IA modeling (i.e., for NLA rather than TATT), obtaining consistent cosmological constraints when different IA prescriptions were assumed. For this reason we use the NLA model as our fiducial choice.

Shear ratio parameters. We include in the analysis galaxy-galaxy lensing small scale information in the form of ratios of galaxy-galaxy lensing measurements [67]. These measurements use as lenses the first three tomographic redshift bins of the MAGLIM lens galaxy sample [92]. When modeling the shear ratio measurements, we marginalize over the uncertainties in the photo-z estimates of the lens samples through a shift $\Delta z^{\rm lens}$ in the mean of the redshift distributions and a stretch $\delta^{\rm lens}$ in their widths,

$$n^{{\rm lens},i}(z) = \delta^{\rm lens}\hat{n}^{{\rm lens},i}(\delta^{\rm lens}[z - \langle z\rangle] + \Delta z^{\rm lens}), \tag{12}$$

where $\langle z\rangle$ is the mean redshift of the lens sample. Priors on $\Delta z^{\rm lens}$ and $\delta^{\rm lens}$ are provided in [93]. We also marginalize over the galaxy-matter bias b_g^i of the three lens samples using broad flat priors.

B. Map making and moments estimator

We describe here how we measure the second and third moments of the convergence field starting from a weak lensing catalog. The following applies to both data and simulated catalogs, as they come in the same format.

Starting from the catalog, we first generate convergence maps for each tomographic bin. The convergence maps used in this work are estimated using a full-sky generalization of the [94] algorithm, first developed by [95]. The map-making process for the DES Y3 convergence maps is explained in full detail in [4], together with a thorough validation of the maps. Here, we briefly summarize the procedure.

We use the weak lensing catalog shear estimates to create pixelized maps for the two components of the shear field. The maps are constructed using HEALPIX with NSIDE = 1024 (corresponding to a pixel size of 3.44 arcmin). The estimated value of the complex shear per pixel is given by

$$\gamma^\nu_{\rm obs} = \frac{\sum_{j=1}^n \epsilon_j^\nu w_j}{\bar{R}\sum_{j=1}^n w_j}, \qquad \nu = 1,2, \tag{13}$$

where ϵ_j is the per-galaxy observed ellipticity, ν refers to the two shear field components, n is the total number of galaxies in the pixel, $\bar{R}$ is the average METACALIBRATION response of the sample ($\bar{R} = 1$ for simulated catalogs), and w_j is the per-galaxy inverse variance weight. The sum runs over all the galaxies in the pixel. Shear maps for each tomographic bins are created. As specified in Sec. III A, we do not explicitly correct for the multiplicative shear bias when making the maps, but rather we account for it during the cosmological inference. Any nonzero mean shear is subtracted from the catalog before creating the maps.

We then convert the shear maps into a curl-free E-mode convergence map $\hat{\kappa}_E$ and a divergence-free B-mode convergence map $\hat{\kappa}_B$ using a spin transformation. This is achieved by using the HEALPIX function MAP2ALM to decompose the shear maps in spherical harmonic space obtaining the coefficients $\hat{\gamma}_{E,\ell m}$, $\hat{\gamma}_{B,\ell m}$, and then calculating $\hat{\kappa}_{E,\ell m}$, $\hat{\kappa}_{B,\ell m}$ as

$$\begin{aligned} \gamma_{\ell m} &= \hat{\gamma}_{E,\ell m} + i\gamma_{B,\ell m} \\ &= -\sqrt{\frac{(\ell+2)(\ell-1)}{\ell(\ell+1)}}(\kappa_{E,\ell m} + i\kappa_{B,\ell m}). \end{aligned} \tag{14}$$

Next we use the HEALPIX function ALM2MAP to convert these coefficients back to real space κ_E and κ_B maps. The maps are smoothed using a top-hat filter and different smoothing scales θ_0. In practice, this is achieved by multiplying the coefficients of the harmonic decompositions of the κ_E and κ_B maps by Eq. (5), prior to the conversion to real space. Simple estimators then give the moments of a smoothed map,

$$\langle \hat{\kappa}^2_{\theta_0} \rangle^{i,j} = \frac{1}{N_{\rm tot}} \sum_{\rm pix}^{N_{\rm tot}} \kappa^i_{\theta_0,{\rm pix}} \kappa^j_{\theta_0,{\rm pix}}, \tag{15}$$

$$\langle \hat{\kappa}^3_{\theta_0} \rangle^{i,j,k} = \frac{1}{N_{\rm tot}} \sum_{\rm pix}^{N_{\rm tot}} \kappa^i_{\theta_0,{\rm pix}} \kappa^j_{\theta_0,{\rm pix}} \kappa^k_{\theta_0,{\rm pix}}, \tag{16}$$

where i, j, k refers to different tomographic bins. We estimate the moments for both the E- and B-mode convergence maps, although only the E-modes moments are used for the cosmological analysis. The sum runs over all the pixels on the sky (thus including regions outside the footprint). This is needed for two reasons; first, the transformation from the shear field to the convergence field is nonlocal and some power is transferred outside the footprint during the transformation, and second, the smoothing of the maps also transfers some of the power from the pixels close to the edge to pixels outside the footprint. We have shown in G20 that our modeling, together with the use of mode-coupling matrices, is able to take into account these effects (also including the lack of shear data outside the footprint, since the shear field is not defined there).

Due to the presence of shape noise, the measurement of galaxy shapes is only a noisy estimate of the shear field γ. This also means that our estimate of the convergence field is noisy,

$$\kappa_{E,{\rm obs}} = \kappa_{E,{\rm true}} + \kappa_{E,{\rm noise}}, \tag{17}$$

$$\kappa_{B,{\rm obs}} = \kappa_{B,{\rm true}} + \kappa_{B,{\rm noise}}. \tag{18}$$

In the above equations, we omitted the smoothing angle θ_0. The contribution of the noise to the convergence field can be estimated by randomly rotating the shapes of the galaxies and applying the full-sky spherical harmonics approach to obtain the convergence [2,7]. As the random rotation should completely erase the cosmological contribution, the resulting convergence signal just contains noise and averages to zero (but with a non-negligible variance).

It follows that when estimating second and third moments from noisy convergence maps, it is necessary to properly denoise the measured moments. Following [7],

$$\langle \kappa^2 \rangle^{i,j} \to \langle \kappa^2 \rangle^{i,j} - \langle \kappa \kappa_{\rm rand} \rangle^{i,j} - \langle \kappa_{\rm rand} \kappa \rangle^{i,j} - \langle \kappa^2_{\rm rand} \rangle^{i,j}, \tag{19}$$

$$\langle \kappa^3 \rangle^{i,j,k} \to \langle \kappa^3 \rangle^{i,j,k} - \langle \kappa^3_{\rm rand} \rangle^{i,j,k} - [\langle \kappa^2_{\rm rand} \kappa \rangle^{i,j,k} - \langle \kappa_{\rm rand} \kappa^2 \rangle^{i,j,k} + {\rm cycl.}], \tag{20}$$

where cycl. refers to the cyclic permutation of the indexes i, j, k for the terms in parenthesis. In the above equations, the term $\langle \kappa^2_{\rm rand} \rangle^{i,j}$ ($\langle \kappa^3_{\rm rand} \rangle^{i,j,k}$) is the noise-only contribution to the second (third) moments of the tomographic bins $i, j, (k)$. Under certain conditions, most of these terms vanish; those terms that do not vanish need to be subtracted from the measured moments. We verified which terms vanish in Appendix D.

IV. LIKELIHOOD AND COVARIANCE

This section provides details about our data vector, likelihood, and covariance. Our data vector consists of all the possible combinations of second and third moments involving the four weak lensing tomographic bins. This adds up to a total of ten combinations of second moments and 20 combinations of third moments. For each of these second and third moments, we consider 10 equally (logarithmic) spaced smoothing scales $\theta_0 \in [3.2, 200]$ arcmin. We then remove scales following G20, i.e., we remove angular scales smaller than a corresponding comoving scale R_0 given by $\theta_0 = R_0/\chi(\langle z \rangle)$, where $\chi(\langle z \rangle)$ is the comoving distance of the mean redshift of a given tomographic bin. In the case of moments from different tomographic bins, we took the average of the mean $\langle z \rangle$ of the two bins. This scale cut is designed to remove scales significantly affected by modeling uncertainties that could contaminate the cosmological analysis, with the dominant uncertainty being contamination due to baryonic effects. G20 determined the fiducial scale cut to be $24h^{-1}$ Mpc when combining second and third moments. We adopt here a scale cut of $28h^{-1}$ Mpc. This change is necessary because the simulated analysis in G20 did not use the final setup for the analysis (e.g., inclusion of the shear-ratio likelihood, final values for redshift distributions, shape noise, effective number densities, covariance, etc.); we therefore repeated the scale cut analysis with all the analysis ingredients updated, and determined $28h^{-1}$ Mpc to be the correct scale cut to be used in this analysis (see Appendix A for more details).

We then compress our data vector using the massively optimized parameter estimation and data compression (MOPED) algorithm [96–98] based on the Karhunen-Loève algorithm, which allows us to reduce the dimensionality of our data vector to the number of model parameters considered. In our case, the number of parameters used to model the moments data vector is 15; therefore, the size of the compressed moments data vector is 15. The compression allows us to reduce the enlargement of the parameters posterior due to noise in the precision matrix estimate, as the covariance matrix is estimated from a limited number of simulations [99]. The final enlargement depends on the size of the compressed data vector rather than on the size of the uncompressed data vector, which makes having an efficient compression scheme desirable. In particular

$$d^{\rm compr}_i = \langle d \rangle^T_{,i} \hat{C}^{-1} d \equiv b_i d, \tag{21}$$

where d is the full-length data vector, $\hat{C}$ is the measurement covariance, and $d^{\rm compr}_i$ is the i-th element of the compressed data vector. The index i refers to the ith model parameter p

considered, and $\langle d \rangle_{,i}^{T}$ is the derivative of the model data vector with respect to that parameter.

We evaluate the posterior of the parameters conditional on the data by assuming a Gaussian likelihood for the data, i.e.,

$$-2 \ln \mathcal{L} = f_2 f_1 [\hat{d} - M(p)] \hat{C}^{-1} [\hat{d} - M(p)]^T. \quad (22)$$

Here $M(p)$ is our theoretical model, $\hat{d}$ is the data vector, and $\hat{C}^{-1}$ is the inverse of our covariance estimate. The posterior is then the product of the likelihood and the priors. Note that the quantities $M(p)$, $\hat{d}$ and $\hat{C}^{-1}$ in Eq. (22) are to be considered compressed quantities. The terms f_1 and f_2 account for noise introduced when the covariance matrix is estimated from random realizations of the data [99–101] and are given by

$$f_1 = \frac{N_{\rm sims} - N_{\rm data} - 2}{N_{\rm sims} - 1}, \quad (23)$$

$$f_2 = \left[1 + \frac{(N_{\rm data} - N_{\rm par})(N_{\rm sims} - N_{\rm data} - 2)}{(N_{\rm sims} - N_{\rm data} - 1)(N_{\rm sims} - N_{\rm data} - 4)} \right]^{-1}, \quad (24)$$

where in our case the number of independent realizations used to estimate the covariance is $N_{\rm sims}$ (i.e., the number of independent simulations) and $N_{\rm data}$ is the length of the data vector. In the case of compressed quantities, f_1, $f_2 \sim 1$ as $N_{\rm sims} \gg N_{\rm data}$.

To correctly infer cosmological parameters from our data, we need an accurate estimate of the measurement uncertainty. Our fiducial method to estimate the covariance uses 1000 independent realizations of the convergence maps generated from the FLASK simulations. As an additional check, we also estimate the covariance using the PKDGRAV and T17 simulations. The PKDGRAV and T17 simulations (Fig. 2) have been produced at cosmologies different to that of the FLASK simulations; hence, these alternative covariances provide extra validation against the dependency of our covariance on the value of cosmological parameters. More details are given in Appendix G. Given a set of N-body simulations, for each realization we measure the second and third moments of the smoothed convergence field and build the covariance matrix as

$$\hat{C} = \frac{1}{\nu} \sum_{i=1}^{\rm N_s} (\hat{d}_i - \hat{d})(\hat{d}_i - \hat{d})^T, \quad (25)$$

where $\nu = {\rm N_s} - 1$ with $\rm N_s$ the number of realizations, $\hat{d}_i$ the data vector measured in the ith simulation, and $\hat{d}$ the sample mean. The data vector is made of a combination of second and third moments as measured at different smoothing scales. We also add to our covariance a "modeling uncertainty" related to the analytical fitting formulas describing the third moments at small scales (see G20 for more details). We then compress the covariance following

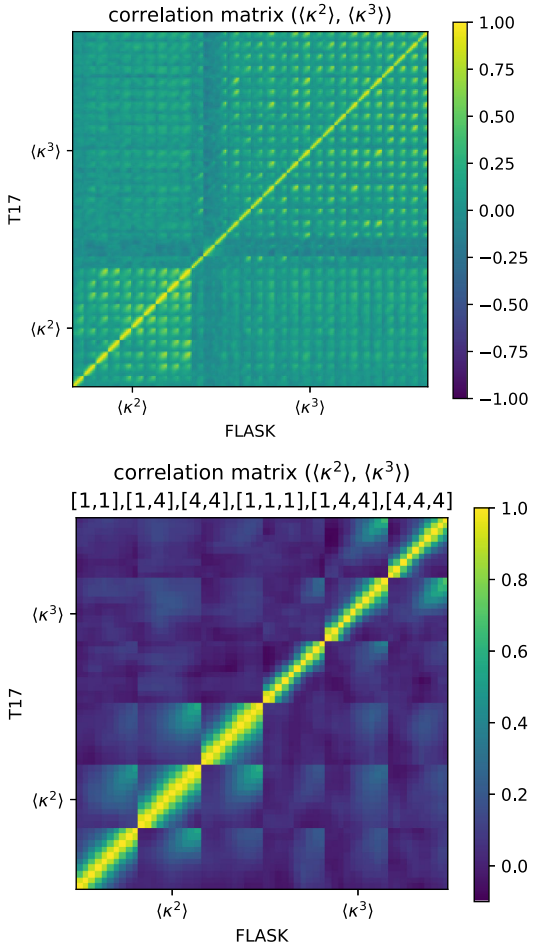

FIG. 2. Top: measured correlation matrix of second and third moments from FLASK simulations (lower right triangle) and from T17 simulations (upper left triangle). No scale cut has been applied. From bottom left to top right, we show the bins: [1, 1], [2, 2], [3, 3], [4, 4], [1, 2], [1, 3], [1, 4], [2, 3], [2, 4], [3, 4], [1, 1, 1], [2, 2, 2], [3, 3, 3], [4, 4, 4], [2, 1, 1], [3, 1, 1], [3, 2, 2], [4, 1, 1], [4, 2, 2], [4, 3, 3], [1, 2, 2], [1, 3, 3], [1, 4, 4], [2, 3, 3], [2, 4, 4], [3, 4, 4], [1, 2, 3], [1, 2, 4], [1, 3, 4], [2, 3, 4]. The main difference between the two covariances is that the FLASK one has on average 5–10% larger amplitude at large scales. The difference vanishes at small scales since those are dominated by shape noise. Bottom: same as the top image, but focusing on a few elements (from bottom left to top right, we show [1, 1], [1, 4], [4, 4] for second moments and [1,1, 1], [1, 4, 4] and [4, 4, 4] for third moments), and showing only the dynamical range [−0.1, 1.0] effectively spanned by the elements of the correlation matrix. The diagonal blocks of the correlation matrix contain essentially all the non-negligible contributions. On large scales, where the cosmic variance contribution to the covariance dominates, the window function of the moments generates off-diagonal terms (within the block diagonal matrix) while on small scales these are due to the pixel window function. Note that in the absence of shape noise we also expect a contribution from nonlinear evolution on small scales.The third moments correlation matrices are more diagonal than second moments ones owing to a larger shape noise contribution. Non-negligible cross-covariance between second and third moments is limited to very large scales, and is generally small (10–15% at most).

$$\hat{C}_{ij}^{\rm compr} = b_i^T \hat{C} b_j. \quad (26)$$

We tested that using the FLASK covariance we were able to correctly recover the input cosmology in simulations (Appendix B).

In the inference, we also add an independent "shear ratio" likelihood [67]. The shear ratio likelihood uses small scale information from the ratio of galaxy-galaxy lensing measurements (the mean tangential shear around lens galaxies) between two weak lensing source tomographic bins and a shared lens sample. Its inclusion improves the constraints on the redshift distributions and on other nuisance parameters of our model. The shear ratio data vector consists of nine scale-averaged ratios. We use as a lens the first three tomographic redshift bins of the MAGLIM lens galaxy sample [92]. The shear ratios likelihood is modeled as an independent Gaussian likelihood, and uses an analytical covariance matrix. The assumption of independency is justified by the smallness of the scales involved in the shear ratio measurements (less than 6 h^{-1} Mpc). We note that the scale cut for this work is 28 h^{-1} Mpc, although the two scale cut limits cannot be directly compared since the mass map smoothing function and the galaxy-galaxy lensing angular bin kernels weight scales slightly differently. Nonetheless, the independency of the shear ratio likelihood has been proven in the context of the DES Y3 3 × 2pt analysis [67]. Because we adopt the same scale cut criteria as the DES 3 × 2pt analysis, we assume independency holds here as well. Lastly, since the shear ratio covariance is analytical, we do not compress the shear ratio data vector.

Having defined the likelihood, we sample the posteriors of our parameters using POLYCHORD [102,103]; this is a nested sampler that uses slice sampling within the nested isolikelihood contours. For the cosmological parameters, we assume a flat ΛCDM cosmology and vary five parameters; $\Omega_{\rm m}$ (the density of the total matter today), σ_8 (the amplitude of structure fluctuations in the present day Universe, parametrized as the standard deviation of the linear overdensity fluctuations on a 8 h^{-1} Mpc scale), $\Omega_{\rm b}$ (the baryonic density in units of the critical density), $n_{\rm s}$ (the spectral index of primordial density fluctuations), and h (the dimensionless Hubble parameter). We assume wide flat priors on $\Omega_{\rm m}$ and σ_8 and adopt the informative priors on h, $n_{\rm s}$, and $\Omega_{\rm b}$ that were used in the DES Y3 2-point function 3 × 2pt analysis (see Table I). When constraining cosmological parameters, we marginalize over nuisance parameters describing mean photo-z uncertainties, multiplicative shear biases and IA effects in our measurements. The modeling of our nuisance parameters is described in Sec. III A. Photo-z uncertainties are parametrized by a shift in the mean of the distribution (one for each tomographic bin). Priors for the shifts come from Myles and Alarcon *et al.* [65]. Multiplicative shear bias priors are described in MacCrann *et al.* [63]. We also assume wide flat priors for intrinsic alignment amplitudes. The addition of the shear-ratio likelihood to the analysis necessitates additional modeling parameters, summarized in Table I. These are lens redshift parameters (modifying the mean redshift and the width of the lens sample redshift distributions) and one free (linear) galaxy bias parameter per lens bin.

Last, we note that since the theory predictions described in Sec. III are time consuming to compute due to the large number of cross-correlations and integrations involved, we implemented an emulator [104,105] to speed up the calculations. In our implementation, the emulator provides fast theoretical predictions by interpolating over a number of predictions computed at a set of training points spanning the parameter space of interest (in our case, the five cosmological parameters). In particular, the quantities emulated are the terms

$$\langle \delta^2_{\theta_0} \rangle^{\rm EE/BB}(\chi) \equiv \sum_\ell \frac{2\ell+1}{4\pi} f_\ell^{-1} W_\ell(\theta_0)^2 \times \sum_{\ell'} M_{\ell\ell'}^{\rm EE/BB,EE} P_{\rm NL}(\ell'/\chi,\chi) F^2_{\ell'} f_{\ell'}, \quad (27)$$

$$\langle \delta^3_{\theta_0} \rangle^{\rm EE/BB}(\chi) \equiv S_3 \times [\langle \delta^2_{\theta_0} \rangle^{\rm EE/BB}(\chi)]^2, \quad (28)$$

which enter in the modeling of Eqs. (2) and (3). The accuracy of the emulator is sufficient to not bias the cosmological analysis, as demonstrated in G20.

V. PREUNBLINDING TESTS

Before proceeding to unblind the data vector and analyse the results of the unblinded analysis, we performed a number of tests. These tests complement the ones performed at the catalog and map level presented in [4,14]. We remind the reader that when this analysis was performed, the shape catalog was already deemed science ready and unblinded, and only the data vector level of blinding was enforced. The whole cosmological pipeline had already been demonstrated in G20 to recover the true cosmology using realistic simulations. We nonetheless repeated the validation in simulations with the updated analysis choices (e.g., redshift distributions, shape noise, priors, etc.) in Appendix B, using both T17 and PKDGRAV simulations. We also slightly changed the scale cut decided in G20, due to updates in the analysis choices. More details concerning the scale cuts are given in Appendix A.

We first performed two tests at the data vector level:

(i) We checked that additive biases due to PSF modeling errors were negligible at the data vector level, i.e., if neglected they would not bias our cosmological analysis. This test is similar to the test performed for the DES Y3 cosmic shear analysis [15]; more details are given in Appendix C.

(ii) We tested that mixed moments between convergence maps E-mode and noise (e.g., $\langle \kappa_N \rangle^{i,j}$) are consistent with expectations based on tests on N-body simulations; more details are given in Appendix D.

We then ran our analysis on blinded data vectors, and checked that:

(i) Cosmological constraints obtained using (blinded) second and third moments were consistent with each other. To this aim, we used posterior predictive distributions (PPD, [106]); see Appendix F.

(ii) The (blinded) posteriors of the systematic parameters did not concentrate at the edge of the prior. The level of agreement/disagreement with the prior was tested using a Gaussian estimator called the "update difference-in-mean" (UDM) statistic [107] (Appendix H).

We then unblinded the data vectors and ran the fiducial analysis; before looking at the unblinded posteriors, we further checked that:

(i) The goodness-of-fit p—value on unblinded data vectors was larger than 1%; see Sec. VI.

(ii) The best-fitting cosmology provided a good description to second and third moments B-modes (which are not included in the data vector), see Appendix E. This was done in an automated fashion such that we did not look at the actual best-fitting values.

In order to quantify goodness-of-fit and internal consistency among different parts of our data vector, we use the PPD methodology developed by [106] and adopted in the main DES Y3 3×2pt analysis. The PPD methodology derives a calibrated probability-to-exceed p; in the case of goodness-of-fit tests, this is achieved by drawing realizations of the data vector for parameters drawn from the posterior under study; for consistency tests (e.g., second moments vs. third moments), the realizations are drawn from disjoint subsets of the data vector. These realizations are then compared to actual observations and a distance metric (χ^2) is computed in data space, which is then used to compute the p-value.

Once all these tests were passed, we looked at the unblinded posteriors of our analysis.

VI. COSMOLOGICAL CONSTRAINTS

We present here the cosmological constraints obtained assuming the ΛCDM model, varying five cosmological parameters and 19 nuisance parameters (10 for the moments likelihood and 9 additional ones for the shear ratio likelihood), as summarized in Table I. In addition to these parameters, we will also quote results in terms of the S_8 parameter, defined as

$$S_8 \equiv \sigma_8(\Omega_m/0.3)^\alpha. \tag{29}$$

The value of α can be chosen such that S_8 best constrains the degeneracy between Ω_m and σ_8. However, the second and third moments have a slightly different degeneracy direction and so there is no value of α that simultaneously optimizes both. For sake of simplicity we adopt $\alpha = 0.5$.

Figure 4 shows the posteriors for S_8, Ω_m, and σ_8 from the second and third moments individually, and from the combinations of the two. Third moments are much less constraining than second moments alone, but they are characterized by a slightly different degeneracy tilt in the σ_8-Ω_m plane compared to second moments. The marginalized mean values of S_8, Ω_m, and σ_8 for the combination of second and third moments, along with the 68% confidence intervals, are

$$\Omega_m = 0.27 \pm 0.03, \tag{30}$$

$$\sigma_8 = 0.83 \pm 0.05, \tag{31}$$

$$S_8 = 0.784 \pm 0.013. \tag{32}$$

We report the constraints from the analysis of second and third moments individually in Table II, and for S_8 we additionally provide a visual comparison in Fig. 5. The combined moments analysis places a 1.7% constraint on S_8 and a 10% constraint on Ω_m, improving by ∼15% and ∼25% over constraints from second moments only. This level of improvement is expected (G20), and is due to the additional non-Gaussian information probed by third moments and the degeneracy breaking when second and third moments are combined. Table II also reports the p-values for the goodness-of-fit tests; these are well above the p-value $= 0.01$ threshold. The unblinded data vectors, along with the best-fitting models from our posteriors, are shown in Fig. 3. We caution the reader from any χ^2-by-eye estimate, as the different scales are highly correlated (especially for second moments, where adjacent scales have a correlations higher than 90%). Constraints from second and third moments are consistent with each other, although it is evident from Fig. 4 that they probe different parts of the parameter space in the σ_8-Ω_m plane.

In Appendix F we use PPD to quantify the internal consistency of our data sets. In particular, we tested the compatibility between second and third moments constraints, between small and large scales, and between parts of the data vector using different redshift bins. These tests were performed prior to unblinding, using blinded data vectors, and were repeated after unblinding (although only the compatibility of second and third moments was considered as an unblinding criterion). In Appendix F we also perform a test analysing the data vector using a different parametrization of the redshift uncertainties, called hyperrank [86].

The results reported here were obtained using the FLASK covariance; in addition, we tested that our results do not change significantly when using the covariances estimated using the T17 or PKDGRAV simulations (Appendix G).

TABLE II. Constraints on the cosmological parameters S_8, Ω_m, and σ_8. For each parameter we report the mean of the posterior and the 68% confidence interval. For the fiducial results (second moments, third moments, and the combination of the two) we also report the PPD goodness-of-fit p-value.

		S_8	Ω_m	σ_8	p-value
Fiducial	Second moments	0.799 ± 0.015	0.21 ± 0.04	0.98 ± 0.10	0.21
	Third moments	0.72 ± 0.05	0.33 ± 0.16	0.73 ± 0.16	0.63
	Second + third moments	0.784 ± 0.013	0.27 ± 0.03	0.83 ± 0.05	0.26
Variations	Second + third moments, no bin 1	0.785 ± 0.014	0.30 ± 0.04	0.79 ± 0.06	
	Second + third moments, no bin 2	0.779 ± 0.015	0.27 ± 0.04	0.83 ± 0.06	
	Second + third moments, no bin 3	0.789 ± 0.019	0.27 ± 0.05	0.83 ± 0.08	
	Second + third moments, no bin 4	0.791 ± 0.018	0.23 ± 0.04	0.92 ± 0.08	
	Second + third moments, hyperrank	0.779 ± 0.014	0.26 ± 0.03	0.83 ± 0.05	
	Second + third moments, small scales	0.780 ± 0.017	0.32 ± 0.05	0.76 ± 0.07	
	Second + third moments, large scales	0.76 ± 0.02	0.28 ± 0.04	0.79 ± 0.07	
	Second + third moments, no shear ratio	0.782 ± 0.017	0.27 ± 0.04	0.83 ± 0.06	
	Second + third moments, FLASK + T17	0.785 ± 0.015	0.27 ± 0.03	0.82 ± 0.06	
	Second + third moments, FLASK + PKDGRAV	0.788 ± 0.015	0.28 ± 0.03	0.82 ± 0.06	
Other works	DES Y3 Cosmic Shear, TATT free neutrino [15,18]	0.772 ± 0.016	0.29 ± 0.05	0.79 ± 0.08	
	DES Y3 Cosmic Shear, NLA fixed neutrino [15,18]	0.788 ± 0.016	0.28 ± 0.04	0.82 ± 0.08	
	DES Y3 3×2pt, TATT free neutrino [108]	0.779 ± 0.014	0.33 ± 0.03	0.74 ± 0.04	
	DES Y3 Peaks + Cls [79]	0.797 ± 0.014	0.28 ± 0.07	0.85 ± 0.11	
	KIDS-1000 [109]	0.751 ± 0.021	0.29 ± 0.08	0.79 ± 0.13	
	HSC Y1 CLs [110]	0.778 ± 0.031	0.18 ± 0.07	1.05 ± 0.16	
	Planck 2018 TT,TE,EE +lowl + lowE [111]	0.834 ± 0.016	0.316 ± 0.008	0.812 ± 0.007	

A. Intrinsic alignment constraints and impact of the shear ratio likelihood

Intrinsic alignment (IA) is a potentially important contribution to the shear signal. We show in Fig. 6 the posterior of the IA amplitude parameter A_{IA} for the combination of second and third moments. Our results are compatible with a null IA signal, as the amplitude of the IA signal is constrained to $A_{IA} = -0.09 \pm 0.17$. Most of the constraint on IA comes from the shear ratio likelihood (Fig. 6), although when performing the analysis without shear ratio we also obtain a null IA signal of $A_{IA} = 0.09 \pm 0.6$. The improvement in the IA constraints due to the inclusion of shear ratio is expected [67]; moreover, because of the slight degeneracy between the IA amplitude parameter and S_8, shear ratio also improves the S_8 constraints (∼25%). The constraints obtained analysing second and third moments only are also very similar: -0.08 ± 0.17 and -0.10 ± 0.15 for second and third moments, respectively. The tighter constraint on A_{IA} from third moments is due to a projection effect related to the broader constraints on Ω_m. These results are compatible with the DES Y3 cosmic shear and 3×2pt analyses results [15,18,108], which also find an IA amplitude consistent with zero. Lastly, we ran an additional test analysing our data vector assuming no IA ($A_{IA} = 0$); the results are shown in Fig. 6 and are almost identical to the fiducial results. The only difference between the no IA model and the fiducial analysis is that the former strongly constrains the nuisance parameter Δz_1 (redshift uncertainty of the first redshift bin). In particular, the posterior of that parameter is shrunk by half, although it is still consistent with zero. The IA model (NLA) used in this work is simpler than the fiducial model (TATT) adopted by the DES Y3 3×2pt analysis [91]. However, [18] finds that simpler IA models such as NLA are sufficient for modeling the DES Y3 data, so we do not think any of the conclusions in this work are affected by our (simpler) IA modeling choice.

B. Comparison with DES constraints

We discuss here how the parameter constraints obtained from this work compare with the ones obtained by other cosmological analyses using DES Y3 data (cosmic shear, 3×2pt, and lensing peaks). Marginalized posteriors for S_8 and Ω_m are shown in Fig. 7 and (for S_8 only) in Fig. 5; we also report the numerical values in Table II. While the level of agreement can be noted in these figures, we cannot quantify it using the PPD metric, as we do not have the cross-covariance of moments with the other data vectors (a requirement of the PPD method).

The comparison that is probably the most relevant is with cosmic shear, which is a two-point correlation of the same lensing field. Our second moment should be consistent with it, although as discussed below the weighting of different scales (in particular in Fourier space) differs. The peaks statistic uses different non-Gaussian information from the third moment, so that is an interesting comparison as well. For completeness we include the 3×2pt results although these use the clustering of lens galaxies (a different probe of the mass distribution). However within the context of

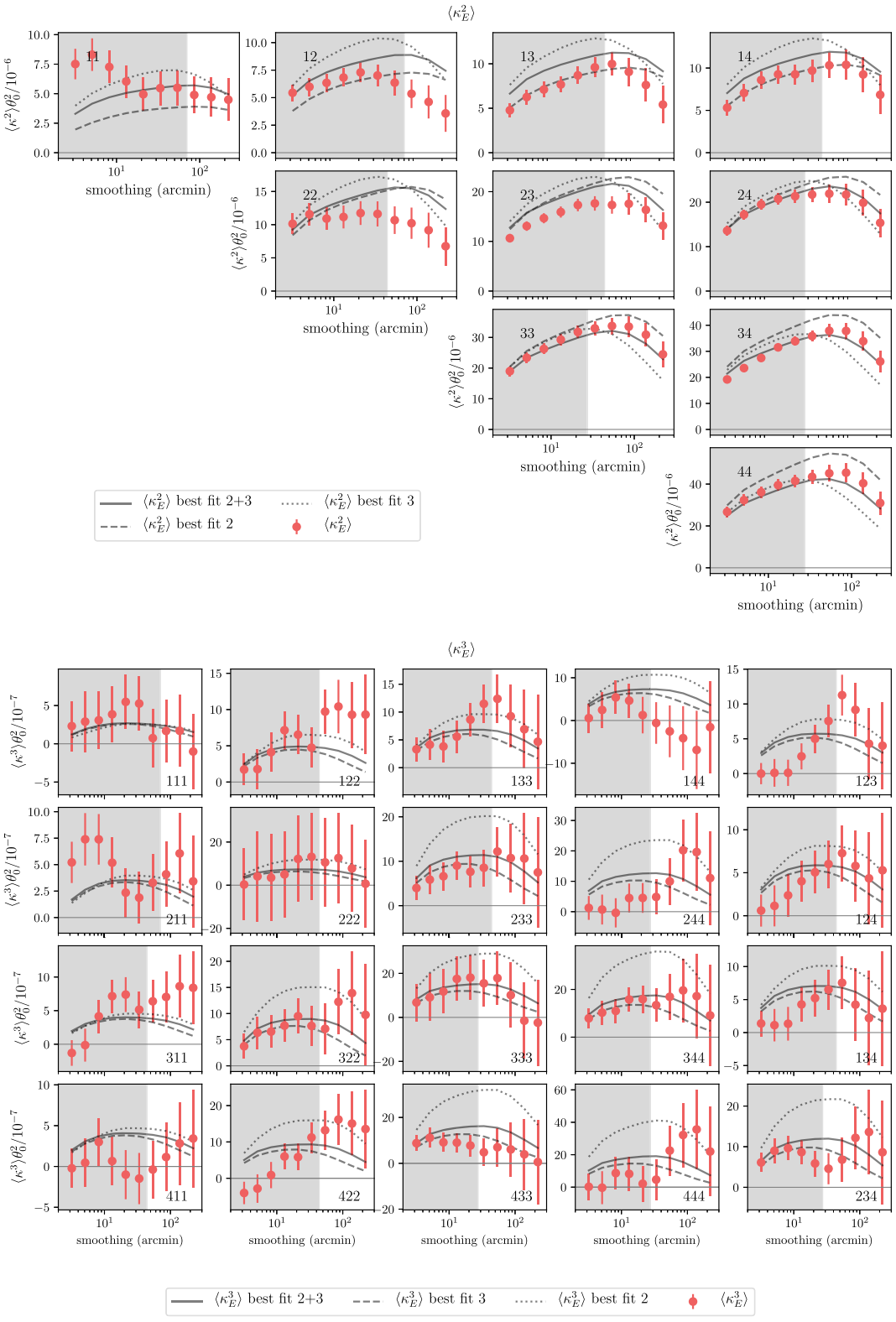

FIG. 3. Measured second moments (upper plots) and third moments (lower plots). Red points represent the measurement. Gray shaded regions highlight the scales removed by the analysis. The conservative scale cut implemented in this analysis removes a large part of our data vector. Solid, dotted, and dashed lines represent the predictions obtained using the best-fitting cosmology of second and third moments analysis (either considered in combinations or alone). Data points are very correlated (Fig. 2), so we caution the reader from any χ^2-by-eye estimation.

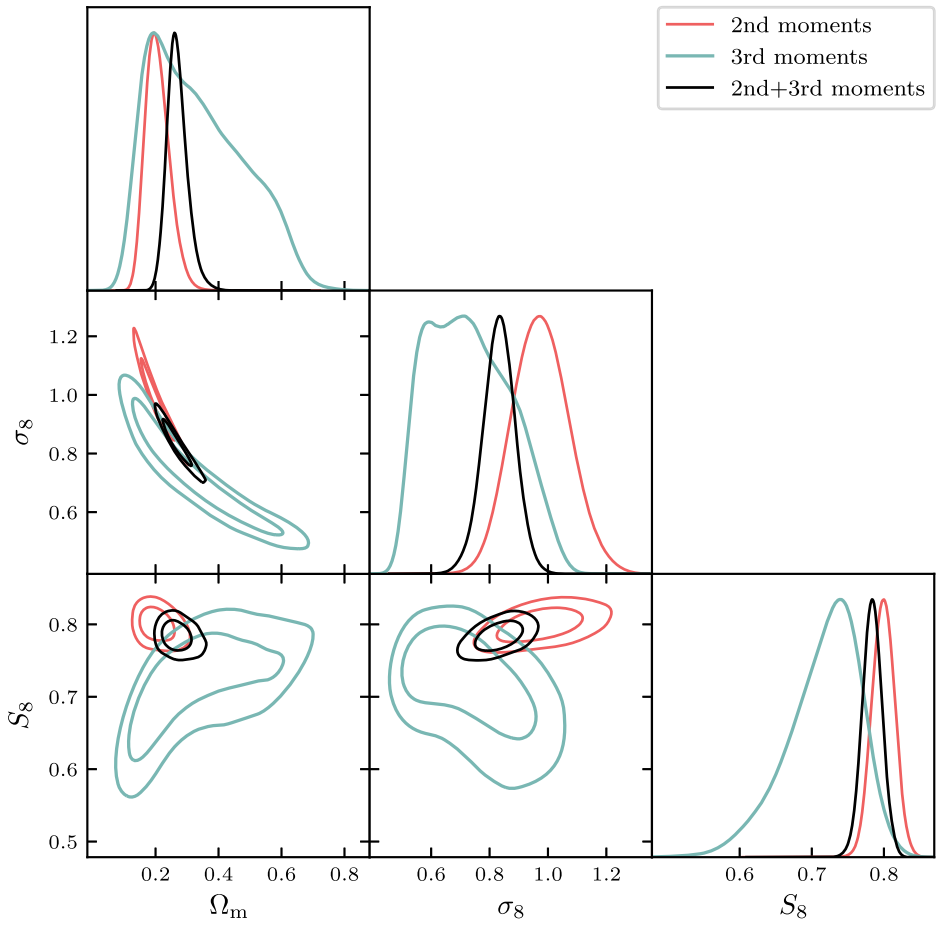

FIG. 4. Posterior distributions of the cosmological parameters Ω_m, σ_8, and S_8 for the second moments, third moments, and the combination of second and third moments. We note that our fiducial analysis include small-scale galaxy-galaxy lensing ratios (a.k.a. shear ratios, Sec. IV). The 2D marginalized contours in these figures show the 68% and 95% confidence levels.

ΛCDM, the results should agree provided the theoretical predictions are accurate and the mitigation of systematic errors in each analysis is reliable.

DES Y3 cosmic shear. The first comparison with other DES Y3 constraints is with the cosmic shear analysis [15,18]. We compare with the constraints from two slightly different cosmic shear analyses: the first one is a ΛCDM analysis which assumes a more complex IA model (the TATT model), and marginalizes over the neutrino mass, whereas the second one, which better matches the analysis choices adopted in this work, assumes NLA as IA model and fixes the neutrino mass to zero.[1] Both adopt the DES Y3 ΛCDM optimized scale cut.[2] The constraints from the combination of second and third moments are in good agreement with the constraints from both cosmic shear analyses.

In terms of constraining power on the S_8 and Ω_m parameters, the NLA + fixed neutrino cosmic shear analysis is similar to the analysis using second moments only. The combined moments analysis is more constraining, due to the additional non-Gaussian information and the degeneracy breaking of the third moments. Although both cosmic shear and second moments are Gaussian statistics and they both probe the shear power spectrum, their posteriors do not have to perfectly overlap, as they weight power spectrum multipoles differently (Appendix I). In particular, our scale cuts exclude some of the higher wave number contributions to ξ_{+-}. Nonetheless, the peaks of the second moments and the combination of second and third moments posteriors are consistent with the peak of the NLA + fixed neutrino cosmic shear posterior in the S_8-Ω_m plane (1σ and 0.15σ, respectively).

DES Y3 3 × 2pt. Similar to the DES Y3 cosmic shear analysis, we compare to two different versions of the DES Y3 3 × 2pt analysis [108]: a first one that assumes ΛCDM,

[1]We remind the reader that neutrinos are not included in the modeling of moments, so their mass is automatically fixed to zero.

[2]The DES Y3 ΛCDM optimized scale cuts are similar to the ones adopted in this work. In particular, they have been chosen so as to have the DES Y3 3 × 2pt S_8-Ω_m constraints unbiased (i.e., $<0.3\sigma$) for a ΛCDM cosmology, with respect to potential baryonic contamination. The scale cuts adopted for the fiducial DES Y3 3 × 2pt results are more conservative because they also consider a *w*CDM cosmology.

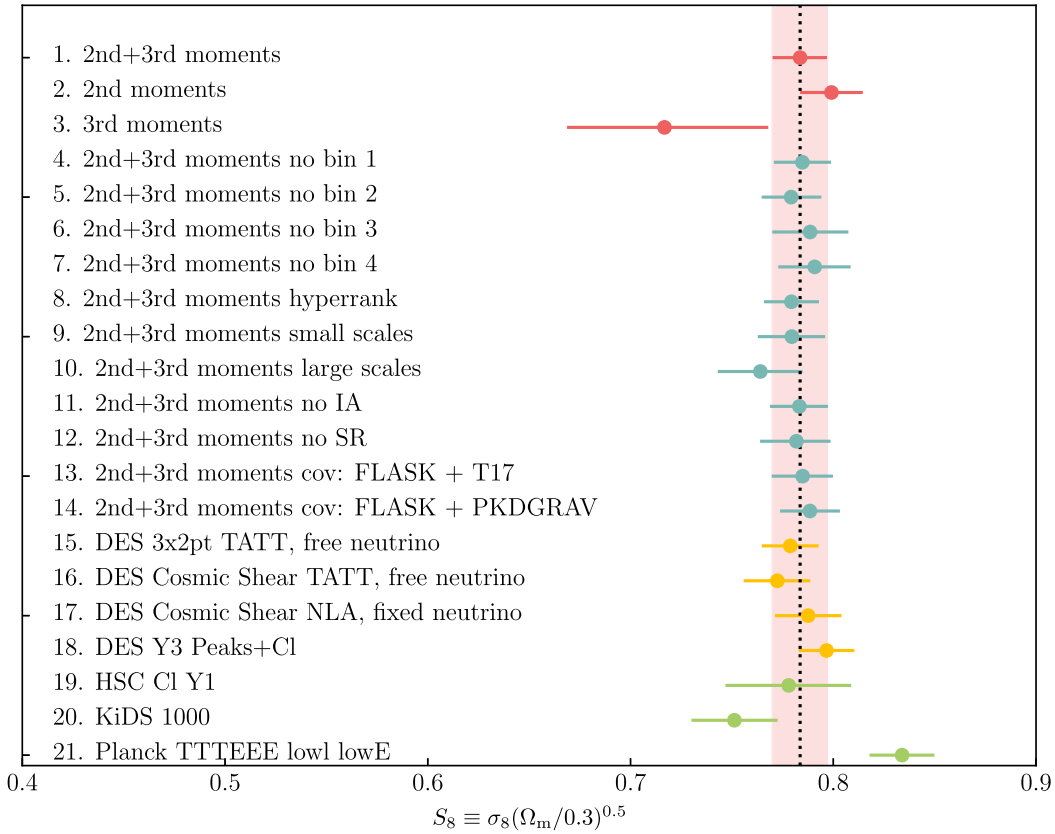

FIG. 5. Constraints on the cosmological parameter S_8; we report the mean of the posterior and the 68% confidence interval. The first three lines are the fiducial results from this analysis. Following that are the S_8 values for a number of variations and systematic tests; removing one redshift bin at a time, using a different parametrization for the redshift distribution called "hyperrank", considering only small or large scales, considering the case with no intrinsic alignement or no shear ratio (SR), and using different covariance matrixes (FLASK + T17 or FLASK + PKDGRAV), as explained in Appendices F and G. Lastly, we compare with a number of results from other works, either with DES or external data.

the TATT model and marginalizes over the neutrino mass, and a second one which better matches the analysis choices adopted in this work, assuming NLA as IA model and fixing the neutrino mass to zero. We report the latter analysis for a visual comparison of the constraining power, but we caution the reader that it is unlikely to pass our scale cuts criteria, which impose a maximum bias of 0.3σ in the S_8-Ω_m plane in case of baryonic contamination. This analysis was not presented in [108], and no adequate scale cut was determined. For sake of simplicity, we decided to use the same scale cut adopted in the 3×2pt TATT + free neutrino mass analysis, which is likely too aggressive. This is because we know that the 3×2pt TATT + free neutrino mass analysis passes the scale cuts criteria with exactly a 0.3σ bias [108]; the NLA + fixed neutrino analysis, having slightly more constraining power, is likely to fail those criteria. To avoid misinterpreting these results, we decided to shift the contours to lie on top of the DES 3×2pt TATT posterior, such that the real position is unknown and the posterior can only be used to get a sense of the effect of different analysis choices on the constraining power of the 3×2pt analysis. The DES 3×2pt analysis relies on three different probes: cosmic shear, galaxy-galaxy lensing, and galaxy clustering. Remarkably, the S_8 constraining power from the moments analysis is 10% better than that from the DES Y3 3×2pt analysis, despite not relying on a lens sample or the 2×2pt part of the data vector. The DES Y3 3×2pt constraints are, however, slightly more stringent in terms of Ω_m (by 10%), due to the significant contribution from the galaxy-galaxy lensing and galaxy clustering part of the analysis. The posteriors show good overlap, with the moments peak being $\sim 1.1\sigma$ away from the DES Y3 3×2pt TATT + free neutrino analysis peak in the S_8-Ω_m plane. Given that the constraints come from different probes we can consider the posteriors to be in reasonably good agreement.

DES Y3 Peaks + Power *spectrum analysis.* [79] use peak counts to extract non-Gaussian information from the convergence field, and combine this with constraints from the power spectrum of convergence maps. The comparison of our analysis with theirs is interesting for two reasons: (1) similar to this analysis, it exploits some non-Gaussian information of the convergence field to constrain cosmological parameters; (2) the Peaks + Power spectrum

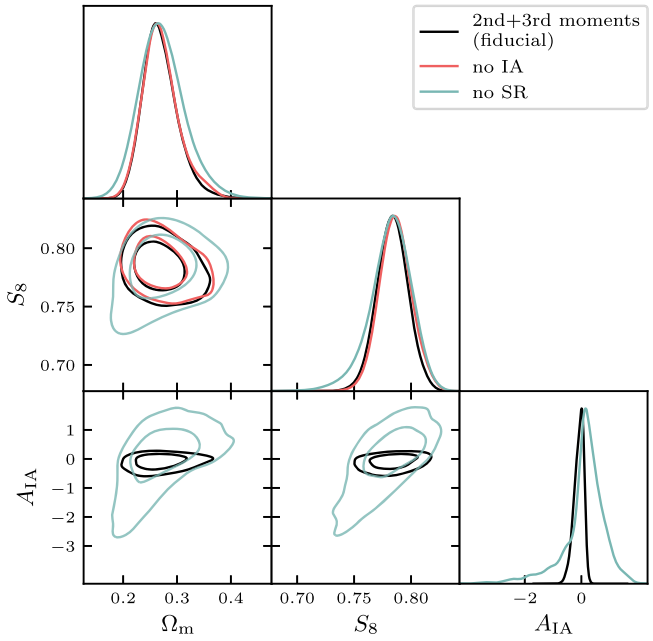

FIG. 6. Posterior distributions of the cosmological parameters $\Omega_{\rm m}$ and S_8, and the IA amplitude parameter $A_{\rm IA}$, for the combination of second and third moments. "SR" stands for shear ratio. The 2D marginalized contours in these figures show the 68% and 95% confidence levels.

analysis uses an independent, completely different framework to provide theory predictions for the observables—they forward model the measurements using a Gaussian process emulator built using N-body simulations of different cosmologies. The analysis choices of the Peaks + Power spectrum analysis and our moments analysis are very similar, the main difference being that the former does not use the shear ratio likelihood and uses somewhat tighter priors for the $n_{\rm s}$, h_{100}, and $\Omega_{\rm b}$ parameters. The results from these two analyses are in agreement (Fig. 7), with the peaks of their posterior within 1σ of ours in the S_8-$\Omega_{\rm m}$ plane. Similar to the moments analysis, the Peaks + Power spectrum analysis finds an IA amplitude consistent with zero.

C. Comparison with external data sets

We compare here our parameter constraints with the results obtained using external data sets. In particular, we compare with the recent results of the KIDS-1000 survey [21], HSC [16], and *Planck* [111]. In order to estimate the tension between different analyses, we calculate a Monte Carlo estimate of the probability of a parameter difference [107,112], using the TENSIOMETER software. In the case of uncorrelated data sets, the probability of the parameter difference reads

$$\mathcal{P}(\Delta\theta) = \int_{V_p} \mathcal{P}_A(\theta)\mathcal{P}_B(\theta - \Delta\theta)d\theta, \tag{33}$$

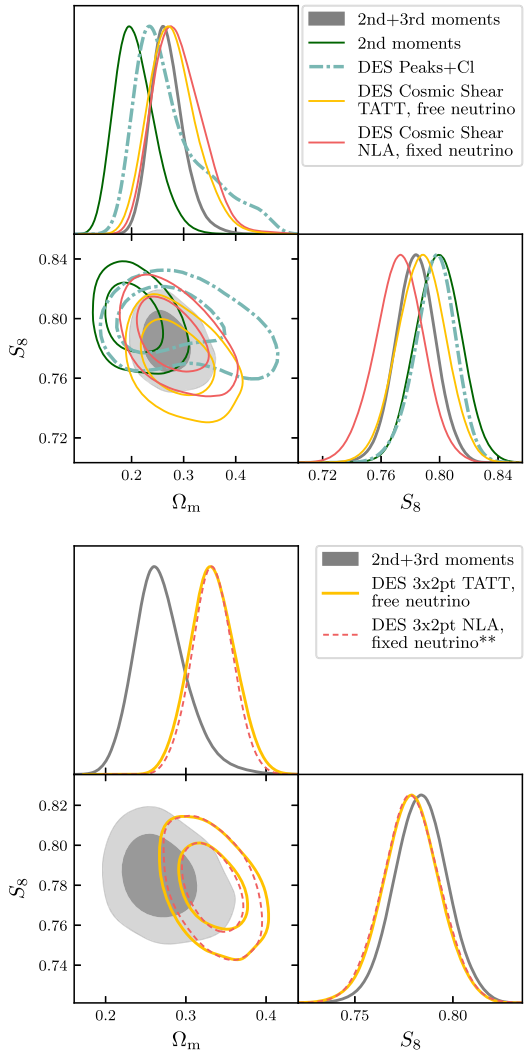

FIG. 7. Posterior distributions of the cosmological parameters $\Omega_{\rm m}$ and S_8. Top panel: we show the posteriors for the moments analysis, two versions of the DES Y3 cosmic shear analysis, and the DES Y3 Peaks + Power spectrum analysis. For readability we do not show the third moments constraints separately. Bottom panel: we show the posteriors for the moments analysis and for two versions of the DES Y3 3 × 2pt analysis. **: the DES 3 × 2pt NLA + fixed neutrino analysis is unlikely to pass our scale cut criteria, see Sec. VI B for more details. For this reason, we shifted the contours on top of the DES 3 × 2 TATT posterior, so as to not unveil the exact location of the (potentially biased) posterior. The 2D marginalized contours in these figures show the 68% and 95% confidence levels.

where V_p is the prior support and $\mathcal{P}_A$ and $\mathcal{P}_B$ are the two posterior distributions of the parameters. The probability of an actual shift in parameter space is obtained from the density of parameter shifts,

$$\Delta = \int_{\mathcal{P}(\Delta\theta)>\mathcal{P}(0)} \mathcal{P}(\Delta\theta)d\Delta\theta, \tag{34}$$

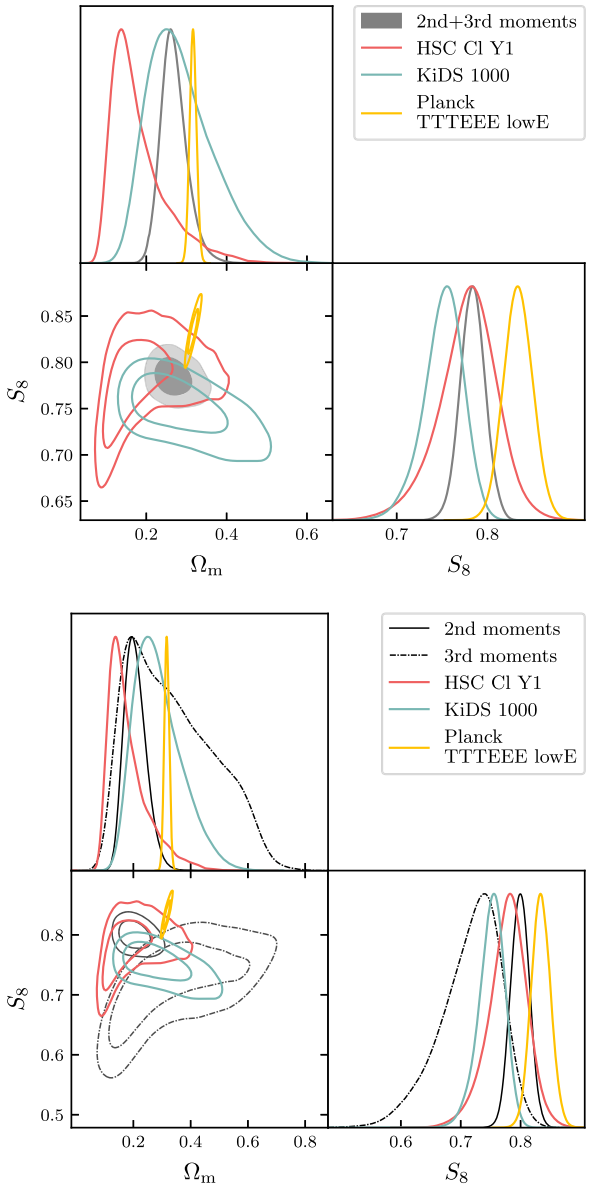

FIG. 8. Posterior distributions of the cosmological parameters Ω_m and S_8, for the moments analysis and for the recent results of the KIDS-1000 survey [21], HSC [16], and *Planck* [111]. Table III shows the tension between the DES moments and other analyses. The upper panel only shows the combination of second and third moments, whereas the lower panel shows second and third moments constraints individually.

which is the posterior mass above the contour of constant probability for no shift, $\Delta\theta = 0$. Due to the discrete nature of our posterior samples, the integral in Eq. (34) is evaluated using a Monte Carlo approach [112].

A visual comparison between the results of the moments analysis and the results obtained from external data sets is provided in Fig. 8 for the S_8 and Ω_m parameters and in Fig. 5 for S_8 only; additionally, the probability of the parameter difference is reported in Table III. The moments analysis is in good agreement with the other weak lensing analyses considered here ($\lesssim 1\sigma$), and it is the most constraining one (owing both to the larger data set and to the extra non-Gaussian information probed by the moments).

TABLE III. Probability of the parameter difference (computed over the full parameter space) between the DES Y3 moments analysis and three analyses using external data sets: KIDS-1000 survey [21], HSC [16], and *Planck* [111].

	Planck TTTEEE lowl lowE	HSC Y1 Power spectrum	KIDS-1000
Second moments	2.7σ	0.3σ	0.9σ
Third moments	2.8σ	1.2σ	0.2σ
Second + third moments	2.2σ	0.9σ	0.6σ

When comparing with the results from the *Planck* analysis, however, we measure a larger tension, at the level of $2.2 - 2.8\sigma$, depending on the combination of moments considered (see Fig. 8). The third moment independently is in 2.8σ tension with *Planck*, which provides a cross-check on the other analyses of 2-point correlations. Note that the joint constraint, though tighter, is in slightly lower tension. Interestingly, the moments analysis is significantly more constraining than *Planck* for the S_8 parameter.

When comparing results from different analyses, we did not try to unify different analysis choices (e.g., priors, scale cuts, etc.); this complicates the comparison [113]. Nevertheless, the moments analysis, in line with other weak lensing analyses, favours lower S_8 values than *Planck*.

VII. SUMMARY

We presented a cosmological analysis of the second and third moments of weak lensing mass (convergence) maps from the Y3 data of the DES. The second moment of the convergence as a function of smoothing scale contains information similar to standard shear 2-point statistics, whereas the third moment, or skewness, contains additional non-Gaussian information. Several theoretical studies have explored the use of statistics beyond 2-point correlations to extract additional non-Gaussian information from lensing data. The 3-point function is the lowest order statistic in perturbation theory and is the simplest to model and interpret. Its signal-to-noise is significantly smaller than for 2-point correlations, but its dependence on the key cosmological parameters (S_8 and Ω_m) differs, enabling partial degeneracy breaking and improved constraints on cosmological parameters. Our study is the first to test these theoretical expectations with data in a comprehensive way, following an end-to-end analysis of mock catalogs that included the expected leading sources of systematic uncertainty (see G20). We note that the counts of peaks in the lensing field are analyzed in a separate DES paper [79] and other non-Gaussian statistics such as the topological

Minkowski functionals as well as deep learning approaches have been proposed as well (see Sec. I for a review).

Our analysis relies on 100 million galaxy shapes measured over 4139 square degrees, which have been used to reconstruct the convergence field in four source redshift bins. The data has been analyzed in the context of the ΛCDM model, varying five cosmological parameters (Ω_m, σ_8, n_s, Ω_b, and h_{100}) and 19 nuisance parameters (modeling astrophysical and measurement uncertainties). One of our goals is to quantify the tension between CMB and late time estimates of S_8 and other relevant parameters. In view of several recent measurements reporting tension between the amplitude of mass fluctuations in the late times vs. early universe (as probed by the CMB), we have carried out measurements and consistency tests of ΛCDM rather than pursue extended cosmological models. The modeling used to describe the second and third moments measured in data is analytical: as described in G20 we have built an emulator to obtain rapid predictions from perturbation theory calculations well tested with N-body simulations. Thus the cosmological analysis here does not rely on large suites of N-body simulations to forward model the signal.

The combined analysis of second and third moments was able to constrain $S_8 \equiv \sigma_8(\Omega_m/0.3)^{0.5}$ with 1.7% uncertainty and Ω_m with 10 percent: in particular, we obtained $S_8 = 0.784 \pm 0.013$ and $\Omega_m = 0.27 \pm 0.03$. The third moments improved the constraints on S_8 and Ω_m by ∼15% and ∼25%, respectively, in line with the expectation based on simulations (G20). The improvement is due to the degeneracy breaking and the non-Gaussian information probed by the third moments. The goodness-of-fit p—value of the data vectors (second, third, and the combination of second and third moments) was found to be way larger than 1%, which is our criterion for a reasonable goodness-of-fit.

We performed our analysis following the blinding scheme proposed by [68]. Before unblinding the analysis, we performed a number of systematic tests which had been defined as unblinding criteria: we checked that additive biases due to PSF modeling errors were small enough to not bias the cosmological analysis; that mixed moments between convergence map E-modes and noise were consistent with expectations based on tests on N-body simulations; that cosmological constraints obtained using second and third moments were consistent with each other using posterior predictive distributions (PPD, [106]); that the best-fitting cosmology provided a good description of the B-modes of the second and third moments as well (the B-modes were not included in the data vector used for the cosmological analysis); that the posteriors of the nuisance parameters did not concentrate at the edge of the prior, tested using the Gaussian estimator update difference-in-mean (UDM) statistic [107]. All these tests were successfully passed. After unblinding, we further used PPD to assess the internal consistency of other subsets of the data vector (small vs. large scales, or across redshift bins); we also tested that our results were robust against different modeling choices for the covariance matrix used in the analysis, or the inclusion of small-scale galaxy-galaxy lensing ratios (a.k.a. shear ratios, [67]). All tests performed after unblinding validated the robustness of our results.

Constraints from the combination of second and third moments were found to be compatible with constraints from the DES Y3 cosmic shear analysis [15,18], the DES Y3 3×2pt analysis [108], and the DES Peaks + Power spectrum analysis [79]. In terms of constraining power, the addition of non-Gaussian information via the third moments in the analysis may be regarded as successful —the constraints on S_8 and Ω_m were shown to be tighter than from DES cosmic shear, and, for S_8, similar to the DES 3×2pt constraint.

We compared our constraints to two contemporaneous lensing surveys: the KIDS-1000 survey [21] and the HSC Y1 data [16], finding agreement ($\lesssim 1\sigma$).

When compared to predictions based on CMB data from the *Planck* satellite [111], we estimate a $2.2 - 2.8\sigma$ tension in the full parameter space, depending on the combination of moments considered (see Table III). The moments analysis favours lower S_8 values compared to *Planck*, in line with other weak lensing analyses. Interestingly the third moment by itself is in tension with Planck at the 2.8σ level: this is significant since additive lensing systematics are more likely to impact the second moment than the third. So the third moment provides a useful check on the "low S_8" cosmic tension between the late time and early universe.

We expect to improve the analysis presented in this work and apply it to future data, such at the final DES Y6 data. Based on the investigation performed in G20 we expect to further improve our constraining power on S_8 by roughly 20%, if we take into account the expected increase in the source number density. We plan to be able to model baryonic effects, which should allow us to push our analysis to smaller scales, improving constraints (up to 20%, Appendix A) and learning about baryonic physics. We are also planning to expand our modeling to include massive neutrinos and the full wCDM parameter space.

The simulated data used in this work has been generated using the public code FLASK (http://www.astro.iag.usp.br/~flask/), the public T17 simulations (http://cosmo.phys.hirosaki-u.ac.jp/takahasi/allsky_raytracing/), and the public code PKDGRAV [72]. The full METACALIBRATION catalog will be made publicly available following publication, at the URL https://des.ncsa.illinois.edu/releases. The code used in this article will be shared on request to the corresponding author.

ACKNOWLEDGMENTS

Funding for the DES Projects has been provided by the U.S. Department of Energy, the U.S. National Science

Foundation, the Ministry of Science and Education of Spain, the Science and Technology Facilities Council of the United Kingdom, the Higher Education Funding Council for England, the National Center for Supercomputing Applications at the University of Illinois at Urbana-Champaign, the Kavli Institute of Cosmological Physics at the University of Chicago, the Center for Cosmology and Astro-Particle Physics at the Ohio State University, the Mitchell Institute for Fundamental Physics and Astronomy at Texas A&M University, Financiadora de Estudos e Projetos, Fundação Carlos Chagas Filho de Amparo à Pesquisa do Estado do Rio de Janeiro, Conselho Nacional de Desenvolvimento Científico e Tecnológico and the Ministério da Ciência, Tecnologia e Inovação, the Deutsche Forschungsgemeinschaft and the Collaborating Institutions in the Dark Energy Survey. The Collaborating Institutions are Argonne National Laboratory, the University of California at Santa Cruz, the University of Cambridge, Centro de Investigaciones Energéticas, Medioambientales y Tecnológicas-Madrid, the University of Chicago, University College London, the DES-Brazil Consortium, the University of Edinburgh, the Eidgenössische Technische Hochschule (ETH) Zürich, Fermi National Accelerator Laboratory, the University of Illinois at Urbana-Champaign, the Institut de Ciències de l'Espai (IEEC/CSIC), the Institut de Física d'Altes Energies, Lawrence Berkeley National Laboratory, the Ludwig-Maximilians Universität München and the associated Excellence Cluster Universe, the University of Michigan, NSF's NOIRLab, the University of Nottingham, The Ohio State University, the University of Pennsylvania, the University of Portsmouth, SLAC National Accelerator Laboratory, Stanford University, the University of Sussex, Texas A&M University, and the OzDES Membership Consortium. Based in part on observations at Cerro Tololo Inter-American Observatory at NSF's NOIRLab (NOIRLab Prop. ID 2012B-0001; PI: J. Frieman), which is managed by the Association of Universities for Research in Astronomy (AURA) under a cooperative agreement with the National Science Foundation. The DES data management system is supported by the National Science Foundation under Grants No. AST-1138766 and No. AST-1536171. The DES participants from Spanish institutions are partially supported by MICINN under Grants No. ESP2017-89838, No. PGC2018-094773, No. PGC2018-102021, No. SEV-2016-0588, No. SEV-2016-0597, and No. MDM-2015-0509, some of which include ERDF funds from the European Union. I. F. A. E. is partially funded by the CERCA program of the Generalitat de Catalunya. Research leading to these results has received funding from the European Research Council under the European Union's Seventh Framework Program (FP7/2007-2013) including ERC Grant agreements No. 240672, No. 291329, and No. 306478. We acknowledge support from the Brazilian Instituto Nacional de Ciência e Tecnologia (INCT) do e-Universo (CNPq Grant No. 465376/2014-2). This manuscript has been authored by Fermi Research Alliance, LLC under Contract No. DE-AC02-07CH11359 with the U.S. Department of Energy, Office of Science, Office of High Energy Physics.

APPENDIX A: SCALE CUTS

We repeat on DES Y3 data the scale cut test we performed on simulated data in G20 in order to determine which part of the data vector can be used in the cosmological analysis. The reason the test is repeated is that some details of the analysis have been updated since G20 (mostly the nuisance parameters priors and the redshift distributions). The scale cut test is performed by contaminating a theory data vector with the known dominant systematic effect that is not part of our model; namely, baryonic feedback based on hydrodynamical simulations as described in G20. Then, we check that the cosmological parameters posterior obtained by analysing the contaminated data vector is not substantially biased with respect to the posterior with an uncontaminated data vector.

We adopted the "optimized scale cut criteria" for the ΛCDM cosmology adopted by the main DES cosmological analysis [15,18,108]. The criterion requires the peak of the marginalized 2D posterior of $\Omega_{\rm m}$ and $S_8 \equiv \sigma_8(\Omega_{\rm m}/0.3)^{0.5}$ obtained by analysing the contaminated data vector to be within 0.3σ of the values obtained with the uncontaminated one. As we partially constrain $n_{\rm s}$, we also require the peak of the marginalized 2D posterior of $n_{\rm s}$ and S_8 to be within 0.5σ of the baseline value. We arbitrarily chose a larger value for the $n_{\rm s}$ and S_8 criteria because n_s is only partially constrained and the posterior might be artificially too sharp. We also note that the DES Y3 3×2pt analysis does not assume any scale cut criteria on n_s. We also check that the χ^2 of the best-fitting cosmology of the analysis of the contaminated data vector is within 0.3 of the expected spread of the χ^2 distribution. Since the length of the compressed data vector is 15, we require the best-fitting $\chi^2 < 1.6$.[3] This second criterion ensures that the best-fitting χ^2 from the analysis on data is unbiased. We note that these last two checks have not been included in the scale cut criteria in the main DES cosmological analysis.

In G20, we determined that a scale cut of $R_0 = 24h^{-1}$ Mpc was sufficient (such that scales smaller than $\theta_0 = R_0/\chi(\langle z\rangle)$ were removed, where $\langle z\rangle$ is the average of the mean redshift of different tomographic bins). When repeating this test, we had to use slightly large scales

[3]Note that we are considering a χ^2 statistic and not a reduced χ^2 statistic. The reported χ^2 might seem small due to the small number of d.o.f (15, due to data-compression) and due to the lack of measurement noise in the input data vectors. For negligible contamination we would expect a best-fit $\chi^2 = 0$ (instead of $\chi^2 \sim$ d.o.f. for a noisy data vector).

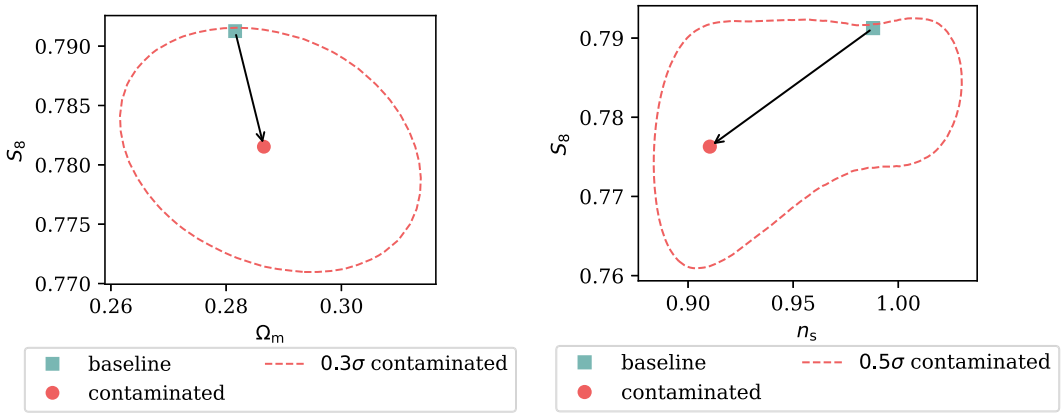

FIG. 9. Parameter posteriors used to determine the scale cuts for the cosmological analysis. Constraints from the combination of second and third moments are shown. "Baseline" refers to an analysis performed on a theory data vector, "Contaminated" refers to the analysis performed on a data vector contaminated by the impact of baryonic feedback (see Appendix A). The dashed lines demarcate the 0.3σ or 0.5σ contours for the 2D marginalized constraints of the contaminated data vector; the filled square and circle show the peak of the posteriors for the contaminated and baseline data vectors, respectively.

($R_0 = 28h^{-1}$ Mpc) to pass the scale cut criteria, due to our updated analysis choices (e.g., inclusion of the shear-ratio likelihood, final values for redshift distributions, shape noise, effective number densities, covariance, etc.). Results are shown in Fig. 9; the peak of the 2D posterior of the contaminated data vector is 0.28σ off the baseline value in the Ω_m-S_8 plane, and 0.48σ in the n_s-S_8 plane; we also obtain a best-fitting $\chi^2 = 0.91 < 1.6$ for the contaminated data vector. Therefore, the scale cut of $R_0 = 28h^{-1}$ Mpc is deemed sufficient.

We note that our scales cut removes a significant number of data points from our measurement. This has a non-negligible impact on our constraining power. Using a simulated data vector, we estimate that we would improve our constraints on S_8 and Ω_m by a further 20% if we could apply no scale cut. This assumes we had a perfect knowledge of the baryonic effects on our data vector, which, unfortunately, is not the case for this analysis.

APPENDIX B: VALIDATION OF THE MODELING ON N-BODY SIMULATIONS

We repeat in this appendix the validation of our theoretical modeling performed in G20. We repeat that validation for two reasons: (1) some of our analysis choices have been updated (e.g., priors, redshift distributions, covariance, etc.); (2) we perform the validation on two independent N-body simulations (whereas in G20 we compared only to one).

We show first in Fig. 10 the comparison between theory predictions and the data vector as measured in the two sets of N-body simulations. For the data vector, we take the average of the data vector measured in every realization available. The mean offset between measurements and predictions is 0.5% and 8% for second and third moments of the T17 simulations, and 0.005% for both second and third moments of the PKDGRAV simulations (note that there are scale dependent residuals that are larger, but they average down when computing a mean offset). Note also that these numbers for the second moments are in agreement with the quoted uncertainties for the power spectrum for the two sets of simulations [71,72]; in particular, the pattern seen for the second moments of the PKDGRAV simulations is similar to that shown in [79].

We used the measured data vector (averaged over all the available realizations) and the scale cut determined in Appendix A to run two simulated cosmological analyses, one for each set of simulations. We compared the posteriors of Ω_m and $S_8 \equiv \sigma_8(\Omega_m/0.3)^{0.5}$ with the posteriors obtained running the same cosmological analysis on a synthetic data vector at the "true" cosmology of the two simulations. Results are shown in Fig. 11, showing a good recovery of the true cosmological parameters.

APPENDIX C: ADDITIVE BIASES DUE TO PSF ERROR

We quantify in this appendix the level of contamination of our data vector due to additive biases related to PSF misestimation. PSF misestimation can cause additive biases in the measured galaxy shapes such that $\boldsymbol{\gamma}^{\rm est} = \boldsymbol{\gamma} + \delta\boldsymbol{e}^{\rm sys}_{\rm PSF} + \delta\boldsymbol{e}^{\rm noise}$. These spurious contributions can be characterized assuming a model for the PSF modeling errors and using a catalog of "reserved" stars that have not been used to train the PSF model. In what follows, we parametrize additive biases due to PSF misestimation following [14,114] (other modeling choices also exist in literature, e.g., [115]). In particular, we assume that

$$\delta\boldsymbol{e}^{\rm sys}_{\rm PSF} = \alpha\mathbf{e}_{\rm model} + \beta(\mathbf{e}_* - \mathbf{e}_{\rm model}) + \eta\left(\mathbf{e}_*\frac{T_* - T_{\rm model}}{T_*}\right), \tag{C1}$$

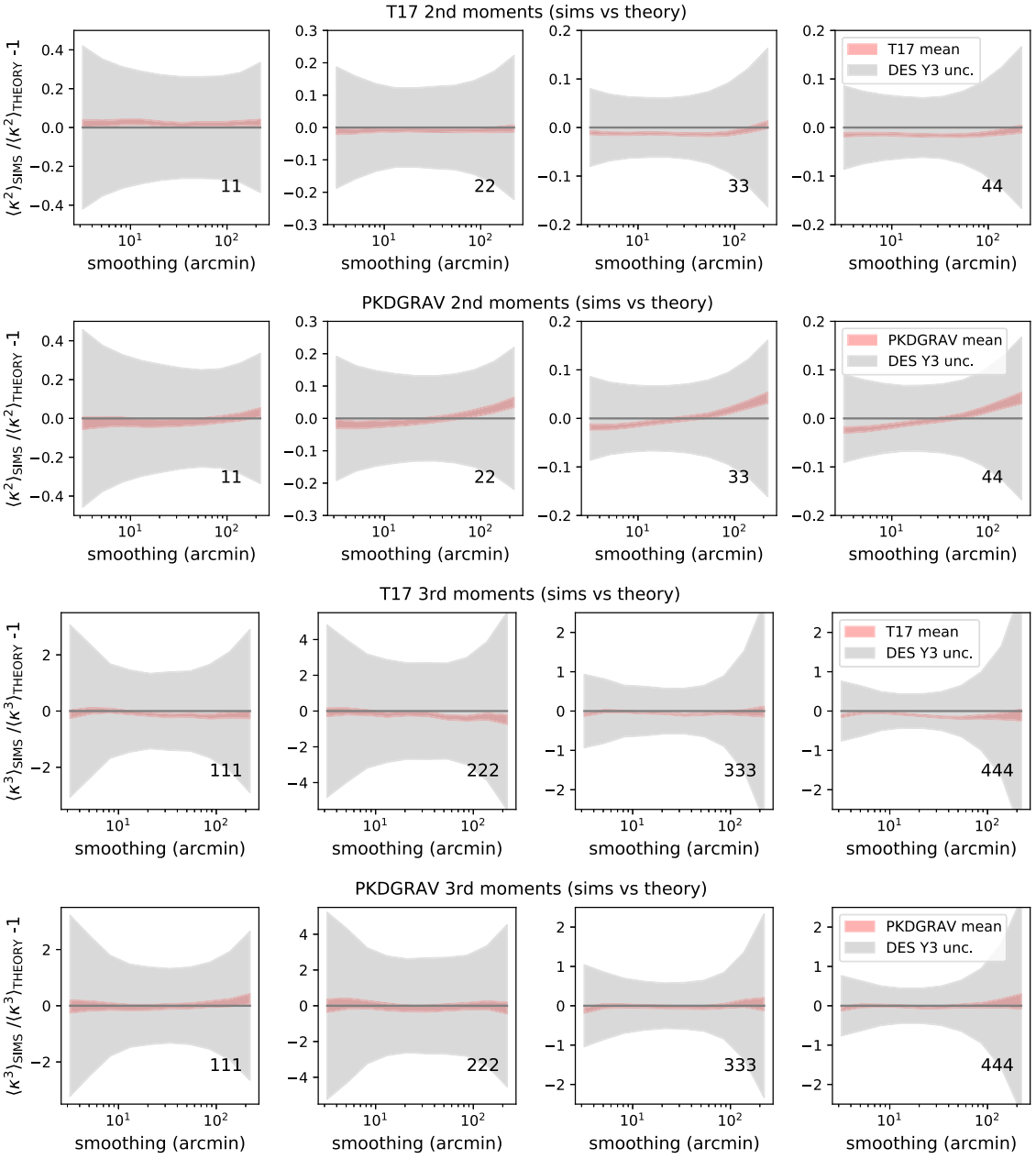

FIG. 10. Comparison between theory predictions and moments as measured in N-body simulations. The red bands encompass the 68 percentile of the moments as measured on all the realizations from the T17 or PKDGRAV simulations. The gray bands represent the expected measurement uncertainty for one individual realization, which represents the DES Y3 survey. No scale cut is applied here. Only "auto" moments are shown. It is evident that the theoretical model agrees with N-body simulations to well within the statistical uncertainty of the survey.

where α, β, and η are coefficients estimated from data, e_* is the PSF ellipticity measured directly using the reserved stars catalog, $T_{\rm model}$ is the modeled PSF size, and T_* is the PSF size measured from the reserved stars catalog. The coefficients α, β, and η for the DES Y3 shape catalog have already been estimated in [14] for the nontomographic case and in [15] for the tomographic case. In what follows, we will use the values from [15], as we are interested in the contamination of our tomographic moments.

An empirical method was used to estimate the contribution to the measured moments due to PSF additive biases. We first created maps of $\mathbf{e}_{\rm model}$, $\mathbf{e}_*$, and $\frac{T_*-T_{\rm model}}{T_*}$ from the reserved stars catalog. Using the estimated values for α, β, and η, we then created maps of $\delta e^{\rm sys}_{\rm model}$, one for each tomographic bin. Last, we computed the second and third moments of the smoothed version of the $\delta \boldsymbol{e}^{\rm sys}_{\rm model}$ maps, in exactly the same way that we estimated the moments of the convergence maps (Sec. III B). In order to estimate the

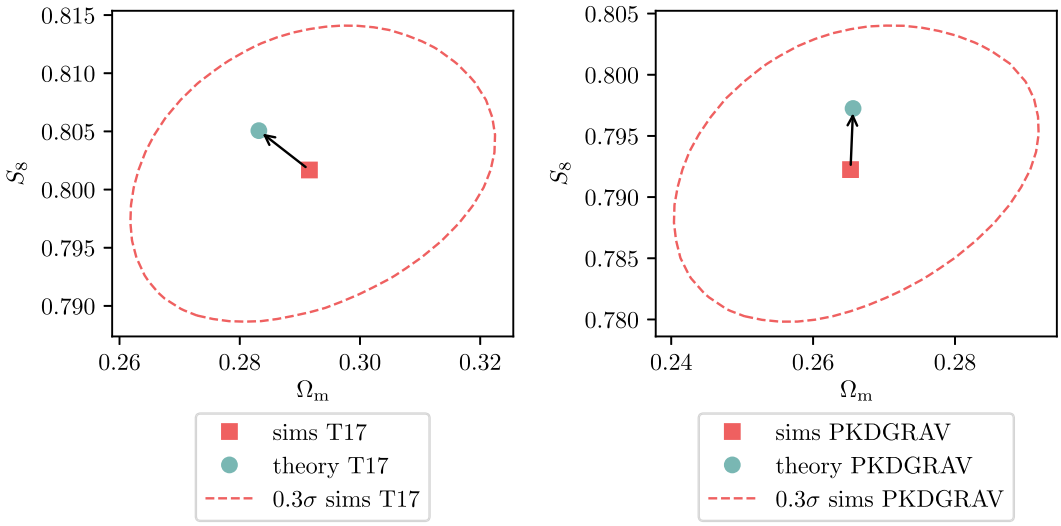

FIG. 11. Parameter posteriors used to validate our modeling of second and third moments with N-body simulations. Constraints from the combination of second and third moments are shown. "Theory" points refer to the peak of the posteriors of the synthetic data vectors computed at the cosmology of either the T17 or PKDGRAV simulation, "sims" squares refer to the peaks of the posteriors of the analyses run on the average data vectors from all the realizations of the N-body simulations. The lines demarcate the 0.3σ contours for the 2D marginalized constraints of the contaminated data vector.

contribution due to noise (that has to be subtracted from the raw, measured moments), we adopted a different technique as the two components of the $\delta\boldsymbol{e}^{\rm sys}_{\rm model}$ field cannot just be randomly rotated as in the case of galaxies. We created two additional versions of the $\delta\boldsymbol{e}^{\rm sys}_{\rm model}$ maps, obtained by sampling two disjoint halves of the reserved stars catalog. We made sure the two halves spanned the footprint uniformly. We then measured the moments of the difference of the two maps, $\delta\boldsymbol{e}^{\rm sys}_{\rm model,DIFF}$. In this way, the true signal should cancel, leaving only a contribution due to noise. The noise contribution to the moments of the $\delta\boldsymbol{e}^{\rm sys}_{\rm model}$ maps can be related to the signal measured from $\delta\boldsymbol{e}^{\rm sys}_{\rm model,DIFF}$ as follows:

$$\langle(\delta\boldsymbol{e}^{\rm sys}_{\rm model,NOISE})^2\rangle^{i,j} = 4\langle(\delta\boldsymbol{e}^{\rm sys}_{\rm model,DIFF})^2\rangle^{i,j}, \quad \text{(C2)}$$

$$\langle(\delta\boldsymbol{e}^{\rm sys}_{\rm model,NOISE})^3\rangle^{i,j,k} = 8\langle(\delta\boldsymbol{e}^{\rm sys}_{\rm model,DIFF})^3\rangle^{i,j,k}, \quad \text{(C3)}$$

for any combination of tomographic bins i, j, and k. The second and third moments contribution due to PSF biases, once the noise term has been subtracted, is shown in Fig. 12. It can be seen clearly that such contribution is subdominant with respect to the moments of the convergence field, and that it mostly affects the large scales of the second moments. To further evaluate the impact of PSF modeling errors, we ran a cosmological analysis on a theory data vector contaminated by the measured moments of the PSF bias, and compared to the results obtained with a cosmological analysis performed on an uncontaminated theory data vector. The results are shown in Fig. 13, demonstrating that PSF additive biases have a negligible impact on our analysis.

APPENDIX D: NOISE TERMS AND SOURCE CLUSTERING

We can only have a noisy estimate of the shear field and so when computing the moments of the convergence maps the contribution due to noise has to be properly subtracted, as explained in Sec. III B [Eqs. (19) and (20)]. It is standard procedure to subtract only the contributions that are known to differ from zero, so as to not unnecessarily inflate the statistical uncertainty of our measurement. We show in Fig. 14 the noise terms as measured from the data. The noise contribution to the convergence map $\kappa_{\rm N}$ has been obtained by randomly rotating the galaxy shapes and repeating the map-making procedure. For the second moments, we do not show the terms $\langle\kappa_{\rm N}\rangle^{i,j}$ when $i = j$, as they are much larger than the measurement $\langle\kappa_{\rm E}\rangle^{i,j}$ (at small scales, they are one order of magnitude larger) and are always subtracted. All the other terms are compatible with zero; the only exception concerns mixed terms of the form $\langle\kappa\kappa^2_{\rm N}\rangle^{i,j,k}$, which presents some deviations from zero at small scales, especially in the moments involving the first tomographic bin (with a significance of $\chi^2 \sim 20$–$25/10$ d.o.f., depending on the bin combinations). This is in line with what we found in simulations in G20, where such terms did not vanish due to correlations between the pixels' shape noise and the shear field value, induced by the intrinsic clustering of the sources [116]. These terms are subtracted from the measured moments before proceeding with the cosmological analysis; due to our scale cut this has a very small impact on the data vector used for the cosmological analysis. By using simulated data vectors with and without source clustering effects, we tested that this procedure is sufficient to remove the effect of source

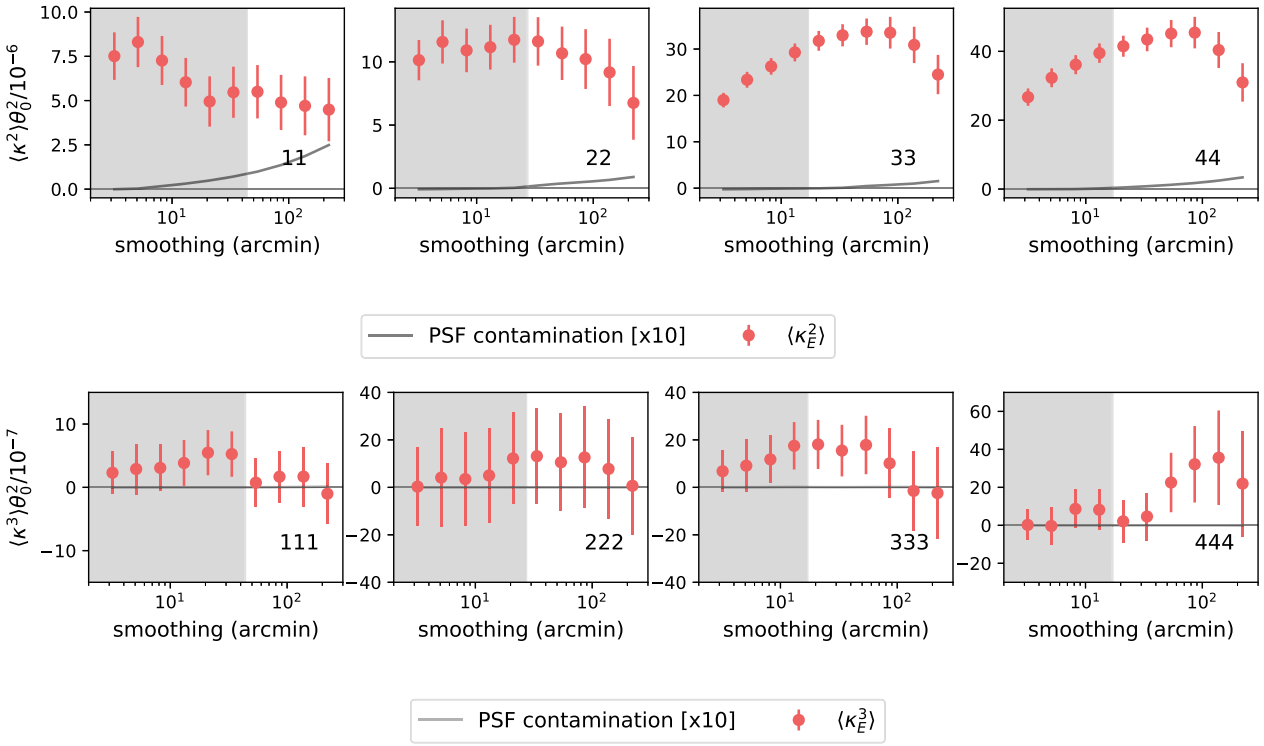

FIG. 12. Contribution of PSF modeling errors to the second and third moments of the convergence fields. The contribution, estimated as explained in Appendix C, is shown as the black lines. Due to its small amplitude, the signal has been multiplied by a factor of 10. The red points represent the measured moments of the convergence field. We only show "auto" moments here, although the pattern is very similar for all the other moments. Gray shaded regions highlight the scales removed by the scale cut used in the analysis.

clustering and to have unbiased cosmological constraints (ignoring source clustering effects produces a shift in 2D Ω_m-S_8 plane of only 0.08σ).

APPENDIX E: B MODES

We show in this appendix the measured moments of the B-modes of the convergence maps. As we used the Kaiser-Squires algorithm to obtain the mass maps, non-null B-modes are expected as a consequence of mask effects [4], and are not necessarily associated with any observational systematic. The measured second moments are shown in Fig. 15. B-modes second moments are significantly nonzero; in the same figure, we also overplot the predicted B-modes given the best-fitting cosmology of the E-modes second moments, showing good agreement with the observed B-modes moments ($\chi^2 = 51/50$ d.o.f.). We do not detect any B-modes third moments at a significant level ($\chi^2 = 127/108$ d.o.f.); this is in line with the expected sensitivity of our data set and with the tests performed in G20.

APPENDIX F: INTERNAL CONSISTENCY TESTS

We quantify here the internal consistency of our data sets. Such tests, which rely on the PPD method, were performed prior to unblinding (using blinded data vectors) and were repeated after unblinding (although only the compatibility of the second and third moments was considered as an unblinding criterion).

Compatibility between second and third moments. This first test was one of the unblinding criteria. Using PPD, we can check that second and third moments posteriors are consistent with each other, so that we can run the analysis using the combined data vector. The PPD p-values for $p(\langle\kappa^2\rangle|\langle\kappa^3\rangle)$ and $p(\langle\kappa^3\rangle|\langle\kappa^2\rangle)$ are reported in Table IV and are well above the $p = 0.01$ threshold. We note that these values need not be the same as the two PPDs are not symmetric.

Redshift tests. Two types of internal consistency checks involving redshift distributions are performed. We performed these checks only using the combination of second and third moments; we did not perform them for second or third moments only.

The first check concerns the impact of removing individual redshift bins from the analysis. In order to perform this test, we again use the PPD. We first repeated our cosmological analysis removing all the second and third moments pairs and triples involving one particular redshift bin. We then sampled from those posteriors (one per bin), and compared using PPD to the observed second and third moments pairs and triples involving that particular redshift bin. This test is meant to highlight potential biases that

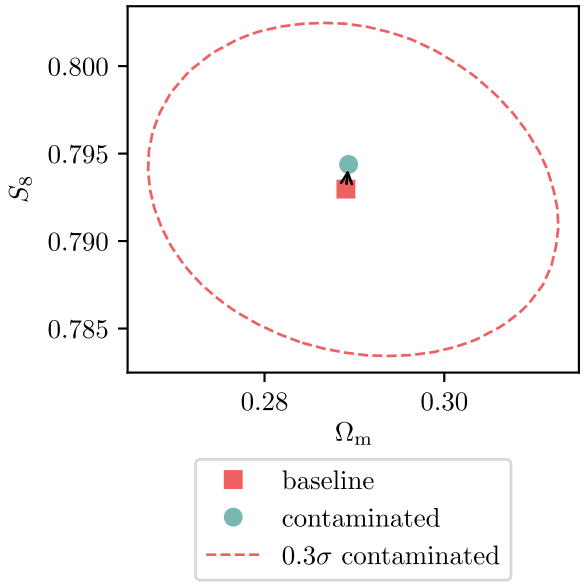

FIG. 13. Parameter posteriors used to determine the level of PSF additive bias contamination. Constraints from the combination of second and third moments are shown. "Baseline" refers to an analysis performed on a theory data vector, "contaminated" refers to the analysis performed on a data vector contaminated by the impact of PSF additive biases (see Appendix C). The dashed lines demarcate the 0.3σ contours for the 2D marginalized constraints of the contaminated data vector; the filled square and circle show the peak of the posteriors.

might preferentially impact the low or high redshift end of our sample. The p-values from the PPD test, for each tomographic bin removed, are reported in Table IV; all the values are safely within our threshold. Fig. 16 shows the peaks of the posteriors in the Ω_m-S_8 plane of the analyses performed removing one bin at a time, and they are within the 1σ contour of the fiducial analysis. The biggest changes are obtained removing bin 4 (the posterior moves towards lower Ω_m values) and removing bin 3 (the constraining power deteriorates more than with the other bins, see Table II). This is not unexpected as bin 3 and 4 are the most constraining ones.

The second test involves using a different parametrization of the redshift uncertainties, called "hyperrank" [86]. With the hyperrank setup, a number of realizations of redshift distributions that encompass the redshift calibration uncertainties are provided. During the cosmological analysis, such realizations are marginalized over, instead of simply marginalizing over the mean of the redshift distributions. Hyperrank is more complete as a method because it also accounts for uncertainties on the higher order moments of the redshift distributions. In the DES Y3 cosmic shear analysis, hyperrank has been proven to deliver very similar results compared to the simpler marginalization over the mean of the redshift distributions [15]. We perform here a similar test, analysing our data vector marginalizing over the hyperrank realizations. The results of this alternative approach are shown in Fig. 16. We measure no significative difference with respect to our fiducial setup, demonstrating that for our analysis marginalizing over the uncertainties of the mean of the redshift distribution is sufficient.

Small scales vs. Large scales. We check for internal consistency between the small and large scales of our data vector. In order to do so, we split our data vector in two halves that have similar constraining power and that retain only either small or large scales. This is achieved by imposing a cut at the comoving scale of $56h^{-1}$ Mpc, which we converted to an angular scale cut as explained in Sec. IV. We use PPD to check for consistency between the two halves of the data vector. The PPD values are reported in Table IV; all the values are safely within our threshold. We note that for this test we considered the combination of second and third moments; we did not perform this test for second or third moments only. We show in Fig. 17 the posterior obtained using the two halves of the data vector; interestingly, the two halves of the data vector are associated to posteriors with a slightly different degeneracy direction in the S_8-Ω_m plane. This is a similar behaviour to what has been found in the DES Y3 cosmic shear analysis [15].

APPENDIX G: TESTS WITH ALTERNATIVE COVARIANCES

We explore in this appendix the effect on our posteriors of using different covariances. We have at our disposal three covariances, obtained using FLASK realizations, T17 N-body simulations, and PKDGRAV N-body simulations. These covariances assume different cosmologies, and in particular, model the higher-order moments of the convergence field slightly differently. This is easy to understand for FLASK covariance, since FLASK assumes the convergence field to be lognormal, which is only an approximation. We should also expect some differences between the T17 and PKDGRAV simulations, based on the different agreement with theory predictions shown in Fig. 11. Such differences probably stem from the different resolution settings of the two sets of N-body simulations.

When using the PKDGRAV and T17 covariances for the inference, we still use the FLASK covariance to compress the data vector since FLASK comes with the largest number of independent realizations.[4] According to [117], this should not bias the inference, but (in the worst case) makes the compression suboptimal. We show in Fig. 18 the posteriors obtained using different covariance matrices

[4]We cannot use PKDGRAV realizations to do the compression, for instance, because the number of independent realizations is similar to (or, depending on the scale cut choice, smaller than) the length of the uncompressed data vector. This would imply that the covariance used for the compression is barely (or not) invertible, making the compression inaccurate (or impossible to be performed).

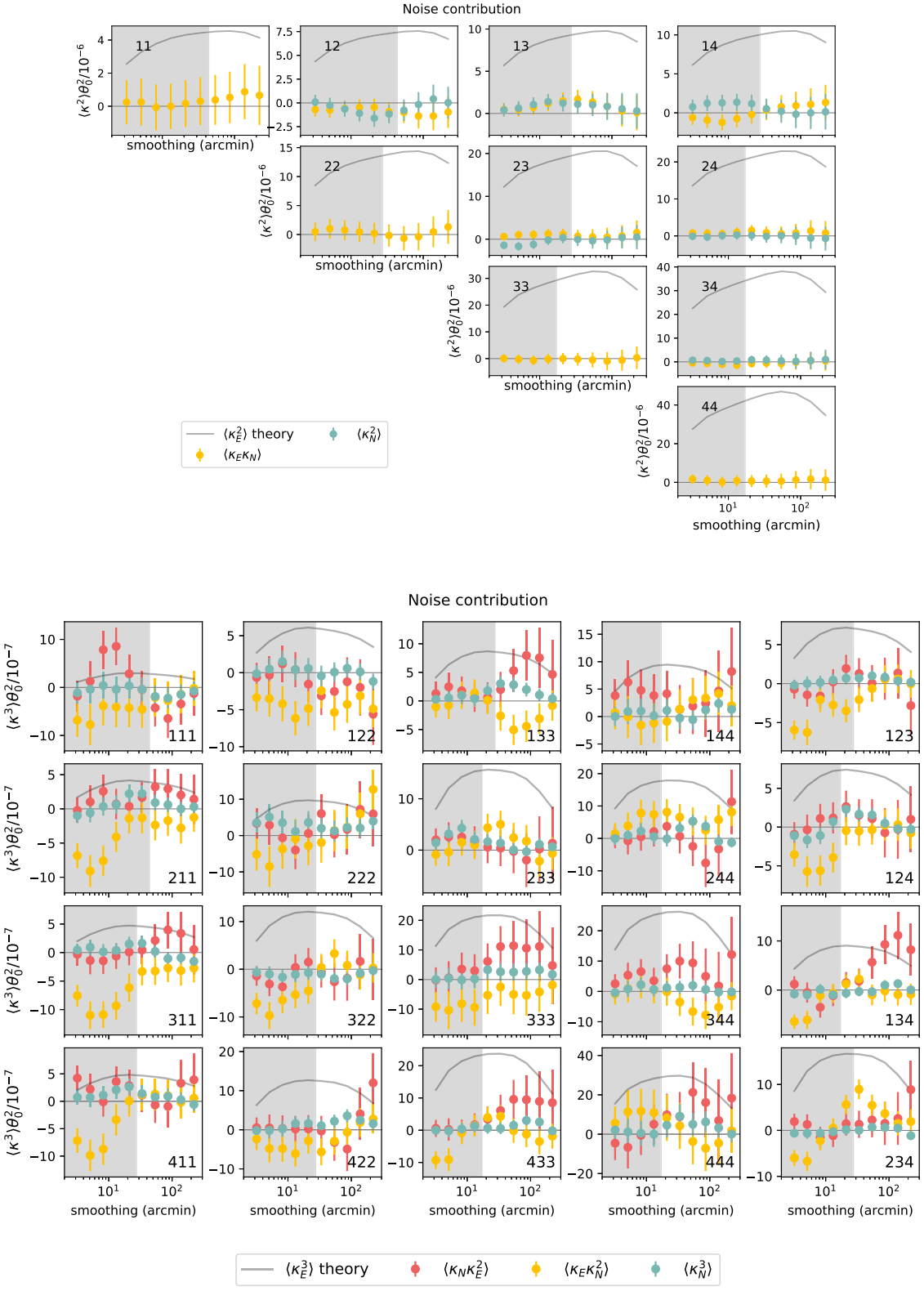

FIG. 14. Measured moments involving the noise contribution to the convergence map. We do not show $\langle\kappa_{\rm N}\rangle^{i,j}$ for $i = j$, as these moments are much larger than the signal $\langle\kappa_{\rm E}\rangle^{i,j}$ and are always subtracted. The gray line is shown for reference and represents the expected theoretical signal for E-mode second and third moments. Gray shaded regions highlight the scales removed by the analysis.

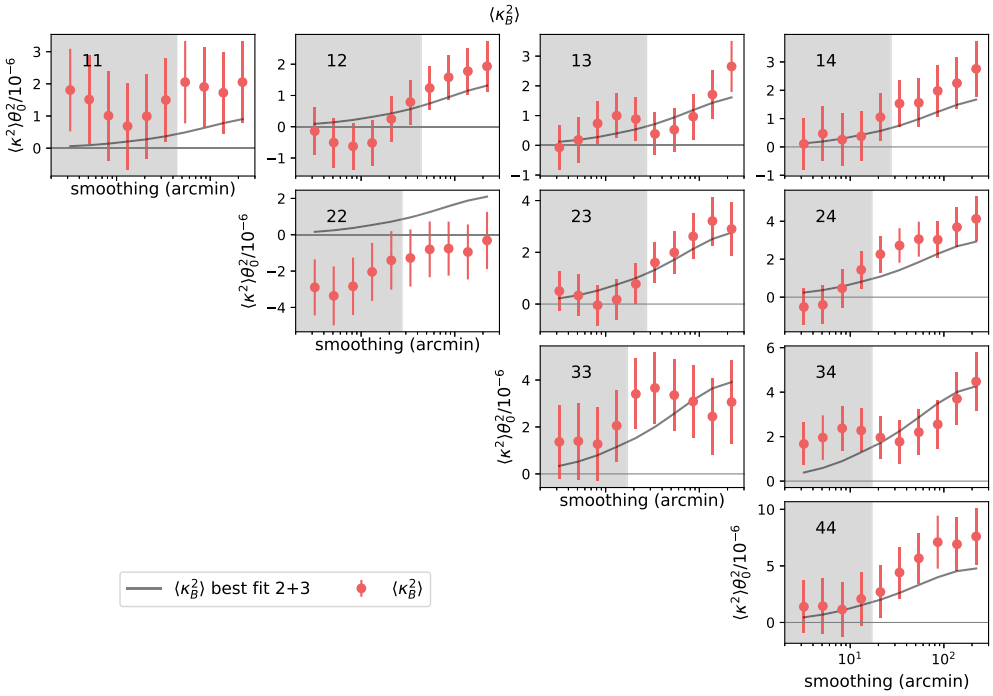

FIG. 15. Measured second and third moments of the B-modes convergence maps. Gray shaded regions highlight the scales removed by the analysis. The solid line represents the predicted B-modes at the best-fitting cosmology of E-modes second and third moments.

for the combined second and third moments on data, and report the values of S_8 in Table II; the posteriors and the values of the constraints are very similar in the three cases, implying that our modeling of the covariance matrix is adequate.

APPENDIX H: PARAMETER 1D POSTERIORS AND TENSION WITH THE PRIORS

We test here whether the best-fitting models are in tension with their priors. This test was performed prior to unblinding. The 1D posteriors and their priors for all the parameters varied in this analysis are shown in Fig. 19. In order to quantify the level of tension with the priors we use

TABLE IV. Summary of internal consistency test p-values. All internal consistency tests pass the predefined (arbitrary) threshold of 0.01. Besides the second vs. third moments tests, all the other tests have been performed on the data vector including the combination of second and third moments.

PPD test	p-values
Data splits	
Bin 1 vs. no bin 1	0.648
Bin 2 vs. no bin 2	0.148
Bin 3 vs. no bin 3	0.659
Bin 4 vs. no bin 4	0.260
Large vs. small scales	0.391
Small vs. large scales	0.350
Second vs. third	0.32
Third vs. second	0.49

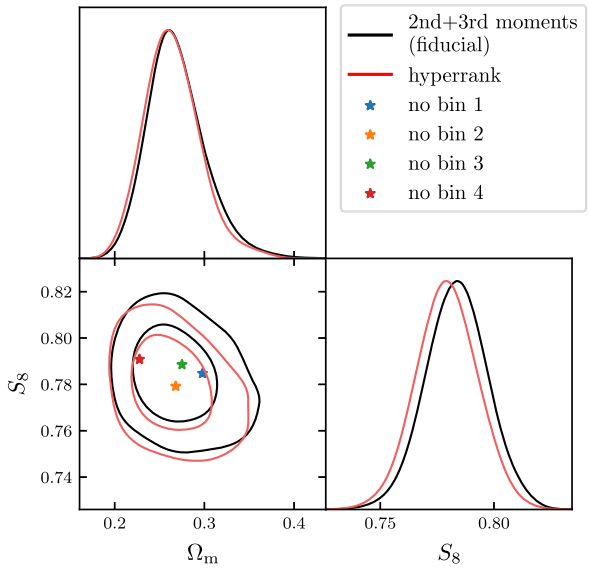

FIG. 16. Posterior distributions of the cosmological parameters Ω_m and S_8 for the combination of second and third moments. We compare the 2D marginalized posterior obtained using hyperrank to model redshift uncertainties to the fiducial results. We also show the peak of the posteriors (the colored stars in the plot) obtained removing one redshift bin at a time from the analysis (and using the fiducial redshift uncertainties model).

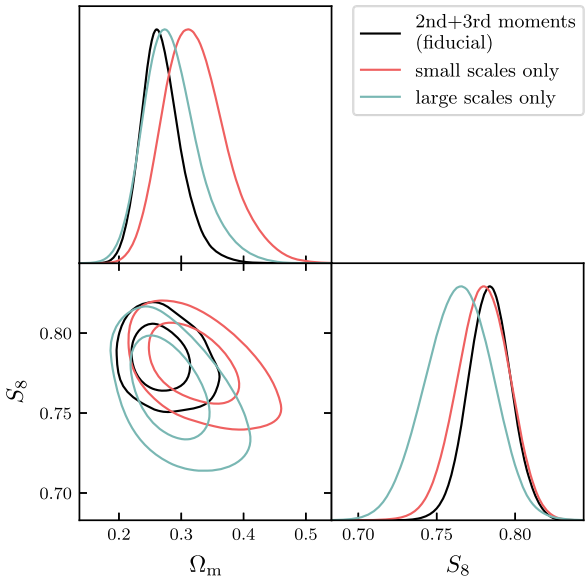

FIG. 17. Posterior distributions of the cosmological parameters Ω_m and S_8 for the combination of second and third moments. The 2D marginalized contours in these figures show the 68% and 95% confidence levels. The figure shows the posteriors obtained using only the small or the large scales of the data vector.

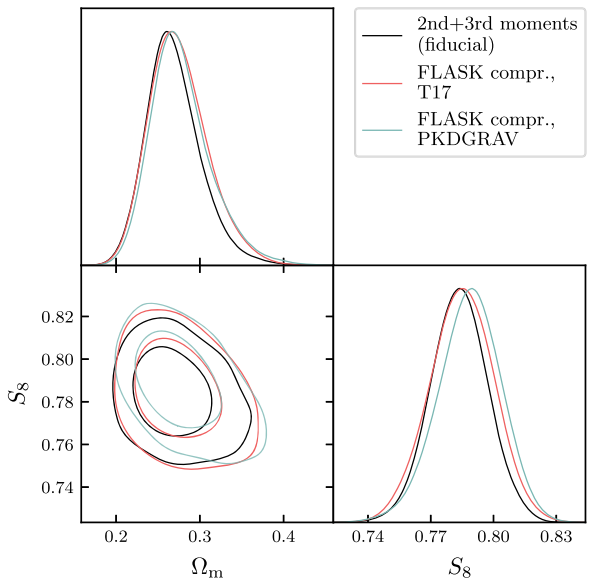

FIG. 18. Posterior distributions of the cosmological parameters Ω_m and S_8 for the combination of second and third moments. The 2D marginalized contours in this figure show the 68% and 95% confidence levels. The figure shows the posteriors obtained using the T17 and PKDGRAV covariances, with the data vector compressed using the FLASK covariance.

a Gaussian estimator called the "update difference-in-mean" (UDM) statistic [107]. The UDM statistic compares the mean parameters from the prior $\hat{\theta}^{\rm p}$ with the updated values $\hat{\theta}^{\rm p+d}$ obtained running the analysis on data. In particular, we can define

$$Q_{\rm UDM} = (\hat{\theta}^{\rm p+d} - \hat{\theta}^{\rm p})^T (\mathcal{C}^{\rm p} - \mathcal{C}^{\rm p+d})^{-1} (\hat{\theta}^{\rm p+d} - \hat{\theta}^{\rm p}), \quad \text{(H1)}$$

where the difference in the mean of the parameters $(\hat{\theta}^{\rm p+d} - \hat{\theta}^{\rm p})$ is weighted by the inverse covariance of the parameters. If the parameters are Gaussian distributed then $Q_{\rm UDM}$ is chi-squared distributed with rank$(\mathcal{C}^{\rm p+d} - \mathcal{C}^{\rm p})$ degrees of freedom. The UDM tension for second moments, third moments, and the combination of second and third moments is 0.6σ, 1.2σ, and 0.8σ, respectively, indicating no tension. We note that most of the parameter posteriors are actually prior dominated (without being in tension with the prior). This is fine as long as we trust our priors. The main parameters constrained by the analysis (σ_8 and Ω_m through S_8, and the intrinsic alignment amplitude $A_{\rm IA}$), however, are not prior dominated. The effective number of parameters $N_{\rm eff}$ constrained by the analysis can be computed as

$$N_{\rm eff} = N - {\rm tr}[(\mathcal{C}^{\rm p})^{-1} \mathcal{C}^{\rm p+d}], \quad \text{(H2)}$$

where N is the number of free parameters in the analysis. For instance, if we restrict to the five cosmological parameters, $N_{\rm eff}$ is only 2.6, 1.5, and 2.6 for second moments, third moments, and the combination of second and third moments, respectively.

APPENDIX I: COMPARISON BETWEEN SECOND MOMENTS AND COSMIC SHEAR WINDOW FUNCTION

We discuss here a potential explanation for the $\sim 1\sigma$ difference between the peaks of the DES Y3 cosmic shear and the second moments analysis in the S_8-Ω_m plane (Fig. 7). Both cosmic shear and second moments are Gaussian statistics and they both probe the shear power spectrum, but their posteriors do not have to perfectly overlap, as they weight power spectrum multipoles differently. Moreover, the process adopted to determine the scales that can be used for each tomographic bin is different for the two analyses; for the moments analysis we adopted a cut based on a well-determined physical scale $\theta_0 = R_0/\chi(\langle z \rangle)$ (Appendix A), whereas the cosmic shear analysis adopted a criterion that evenly distributed a given $\Delta\chi^2$ among tomographic bins (where the $\Delta\chi^2$ is computed between a synthetic data vector contaminated with baryonic effects and an uncontaminated data vector). Although both criteria are designed to minimize the impact of baryons on the S_8-Ω_m constraints, they can contribute to the different

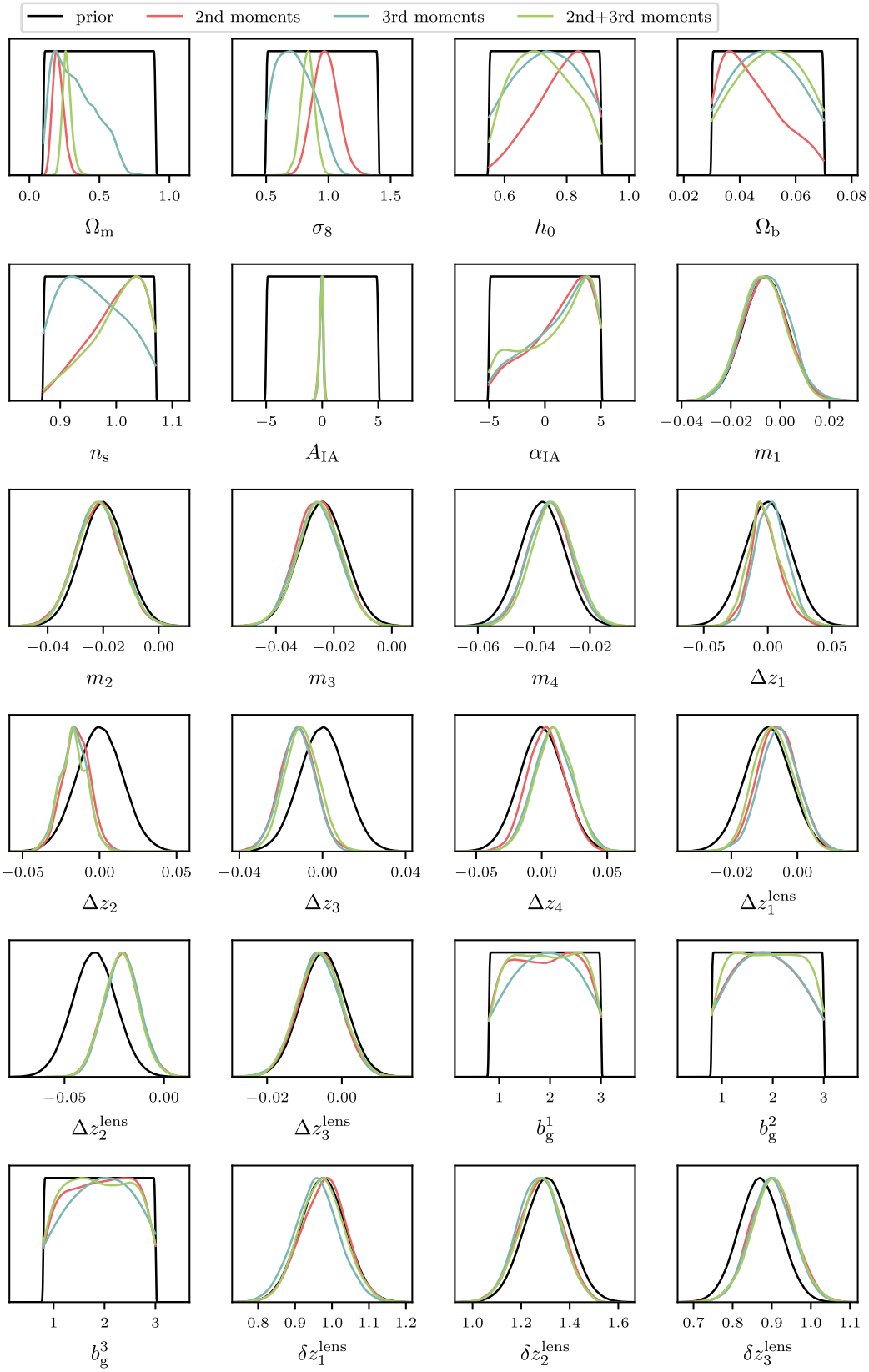

FIG. 19. 1D marginalized posteriors for each parameter varied in the cosmological analysis. We show posteriors for second moments, third moments, and the combination of second and third moments, and compare them with their prior. Note that in some cases the edges of the 1D posteriors might look to extend over the prior edges; however, it is only a visual effect due to the smoothing of the plotting script close to the edge of the prior.

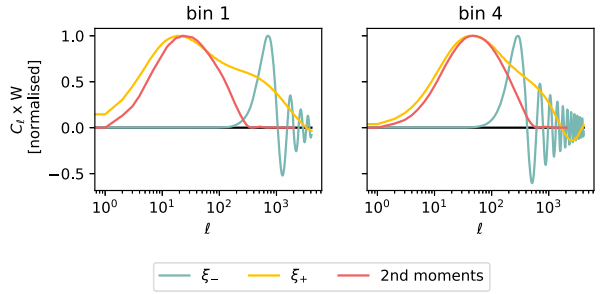

FIG. 20. Shear power spectrum for a given redshift bin multiplied by the window function W of a given statistics (second moments, ξ_{+-}), normalized to their maximum value. For each statistics, the window function is computed at the minimum angular or smoothing scale allowed by the scale cut. The window functions for ξ_{+-} are defined as $J_{0/4}(\ell\theta)$, whereas the second moments window function is $(2\ell+1)[W_\ell(\theta_0)]^2$, with $W_\ell(\theta_0)$ given by Eq. (5). For second moments, we also convolved the power spectrum by the mode-coupling matrix.

sensitivity of the statistics to the shear power spectrum multipoles.

Figure 20 shows, for the first and the last redshift bins, how the different statistics weight the multipoles of the shear power spectrum at the minimum angular scale allowed by their scale cut. The cosmic shear scale cut allows ξ_{+-} to probe significantly higher multipoles compared to the second moments, whose window function is more compact. When considering the redshift bin 1 (4), ∼30 (∼25) per cent of the S/N of the ξ_{+-} data vector passing the scale cut comes from $\ell > 200$. For second moments the contribution to the S/N from $\ell > 200$ is significantly smaller; ∼1 (∼10) per cent. Although a more quantitative assessment of the compatibility between the second moments and cosmic shear constraints should be performed via PPD, we consider the pieces of evidence provided in this appendix sufficient to justify the differences between the two analyses shown in Fig. 7.

[1] A. Einstein, Science **84**, 506 (1936).
[2] C. Chang, A. Pujol, B. Mawdsley *et al.*, Mon. Not. R. Astron. Soc. **475**, 3165 (2018).
[3] C. Chang, V. Vikram, B. Jain *et al.*, Phys. Rev. Lett. **115**, 051301 (2015).
[4] N. Jeffrey, M. Gatti, C. Chang *et al.*, Mon. Not. R. Astron. Soc. **505**, 4626 (2021).
[5] J. Liu, A. Petri, Z. Haiman, L. Hui, J. M. Kratochvil, and M. May, Phys. Rev. D **91**, 063507 (2015).
[6] M. Oguri, S. Miyazaki, C. Hikage *et al.*, Publ. Astron. Soc. Jpn. **70**, S26 (2018).
[7] L. Van Waerbeke, J. Benjamin, T. Erben *et al.*, Mon. Not. R. Astron. Soc. **433**, 3373 (2013).
[8] V. Vikram, C. Chang, B. Jain *et al.*, Phys. Rev. D **92**, 022006 (2015).
[9] Dark Energy Survey Collaboration, Mon. Not. R. Astron. Soc. **460**, 1270 (2016).
[10] K. Kuijken, C. Heymans, H. Hildebrandt *et al.*, Mon. Not. R. Astron. Soc. **454**, 3500 (2015).
[11] H. Aihara, N. Arimoto, R. Armstrong *et al.*, Publ. Astron. Soc. Jpn. **70**, S4 (2018).
[12] P. A. Abell, J. Allison *et al.* (LSST Science Collaboration), arXiv:0912.0201.
[13] R. Laureijs, J. Amiaux, S. Arduini *et al.*, arXiv:1110.3193.
[14] M. Gatti, E. Sheldon, A. Amon *et al.*, Mon. Not. R. Astron. Soc. **504**, 4312 (2021).
[15] A. Amon, D. Gruen, M. A. Troxel *et al.*, Phys. Rev. D **105**, 023514 (2022).
[16] C. Hikage, M. Oguri, T. Hamana *et al.*, Publ. Astron. Soc. Jpn. **71**, 43 (2019).
[17] H. Hildebrandt, M. Viola, C. Heymans *et al.*, Mon. Not. R. Astron. Soc. **465**, 1454 (2017).
[18] L. F. Secco, S. Samuroff, E. Krause *et al.*, Phys. Rev. D **105**, 023515 (2022).
[19] M. A. Troxel, N. MacCrann, and J. Zuntz *et al.*, Phys. Rev. D **98**, 043528 (2018).
[20] T. Hamana, M. Shirasaki, S. Miyazaki *et al.*, Publ. Astron. Soc. Jpn. **72**, 16 (2020).
[21] M. Asgari, C.-A. Lin, B. Joachimi *et al.*, Astron. Astrophys. **645**, A104 (2021).
[22] P. Coles and B. Jones, Mon. Not. R. Astron. Soc. **248**, 1 (1991).
[23] E. Hubble, Astrophys. J. **79**, 8 (1934).
[24] V. Wild, J. A. Peacock, O. Lahav *et al.*, Mon. Not. R. Astron. Soc. **356**, 247 (2005).
[25] L. Clerkin, D. Kirk, M. Manera *et al.*, Mon. Not. R. Astron. Soc. **466**, 1444 (2017).
[26] M. Gatti, C. Chang, O. Friedrich *et al.*, Mon. Not. R. Astron. Soc. **498**, 4060 (2020).
[27] A. Petri, J. Liu, Z. Haiman, M. May, L. Hui, and J. M. Kratochvil, Phys. Rev. D **91**, 103511 (2015).
[28] S. Vafaei, T. Lu, L. van Waerbeke, E. Semboloni, C. Heymans, and U.-L. Pen, Astropart. Phys. **32**, 340 (2010).
[29] D. Zürcher, J. Fluri, R. Sgier, T. Kacprzak, and A. Refregier, J. Cosmol. Astropart. Phys. 01 (2021) 028.
[30] V. F. Cardone, S. Camera, R. Mainini , A. Romano, A. Diaferio, R. Maoli, and R. Scaramella, Mon. Not. R. Astron. Soc. **430**, 2896 (2013).
[31] A. Peel, V. Pettorino, C. Giocoli, J.-L. Starck, and M. Baldi, Astron. Astrophys. **619**, A38 (2018).
[32] V. Ajani, A. Peel, V. Pettorino, J.-L. Starck, Z. Li, and J. Liu, Phys. Rev. D **102**, 103531 (2020).
[33] J. P. Dietrich and J. Hartlap, Mon. Not. R. Astron. Soc. **402**, 1049 (2010).

[34] T. Kacprzak, D. Kirk, O. Friedrich *et al.*, Mon. Not. R. Astron. Soc. **463**, 3653 (2016).
[35] J. M. Kratochvil, Z. Haiman, and M. May, Phys. Rev. D **81**, 043519 (2010).
[36] N. Martinet, P. Schneider, H. Hildebrandt *et al.*, Mon. Not. R. Astron. Soc. **474**, 712 (2018).
[37] H. Shan, X. Liu, H. Hildebrandt *et al.*, Mon. Not. R. Astron. Soc. **474**, 1116 (2018).
[38] M. Vicinanza, V. F. Cardone, R. Maoli, R. Scaramella, and X. Er, arXiv:1606.03892.
[39] M. Vicinanza, V. F. Cardone, R. Maoli, R. Scaramella, and X. Er, Phys. Rev. D **97**, 023519 (2018).
[40] L. Fu, M. Kilbinger, T. Erben *et al.*, Mon. Not. R. Astron. Soc. **441**, 2725 (2014).
[41] E. Semboloni, T. Schrabback, L. van Waerbeke, S. Vafaei, J. Hartlap, and S. Hilbert, Mon. Not. R. Astron. Soc. **410**, 143 (2011).
[42] M. Takada and B. Jain, Mon. Not. R. Astron. Soc. **344**, 857 (2003).
[43] M. Takada and B. Jain, Mon. Not. R. Astron. Soc. **348**, 897 (2004).
[44] J. M. Kratochvil, E. A. Lim, S. Wang, Z. Haiman, M. May, and K. Huffenberger, Phys. Rev. D **85**, 103513 (2012).
[45] C. Parroni, V. F. Cardone, R. Maoli, and R. Scaramella, Astron. Astrophys. **633**, A71 (2020).
[46] M. Vicinanza, V. F. Cardone, R. Maoli, R. Scaramella, X. Er, and I. Tereno, Phys. Rev. D **99**, 043534 (2019).
[47] J. Fluri, T. Kacprzak, A. Lucchi, A. Refregier, A. Amara, T. Hofmann, and A. Schneider, Phys. Rev. D **100**, 063514 (2019).
[48] J. Fluri, T. Kacprzak, A. Refregier, A. Amara, A. Lucchi, and T. Hofmann, Phys. Rev. D **98**, 123518 (2018).
[49] N. Jeffrey, J. Alsing, and F. Lanusse, Mon. Not. R. Astron. Soc. **501**, 954 (2020).
[50] D. Ribli, B. Á. Pataki, and I. Csabai, Nat. Astron. **3**, 93 (2019).
[51] P. Fosalba, E. Gaztañaga, F. J. Castander, and M. Manera, Mon. Not. R. Astron. Soc. **391**, 435 (2008).
[52] E. Gaztanaga and F. Bernardeau, Astron. Astrophys. **331**, 829 (1998).
[53] B. Jain and U. Seljak, Astrophys. J. **484**, 560 (1997).
[54] A. Pujol, C. Chang, E. Gaztañaga *et al.*, Mon. Not. R. Astron. Soc. **462**, 35 (2016).
[55] B. Flaugher, H. T. Diehl, K. Honscheid *et al.*, Astron. J. **150**, 150 (2015).
[56] Dark Energy Survey Collaboration, Astrophys. J. Suppl. Ser. **239**, 18 (2018).
[57] E. Morganson, R. A. Gruendl, F. Menanteau *et al.*, Publ. Astron. Soc. Pac. **130**, 074501 (2018).
[58] I. Sevilla *et al.*, arXiv:1109.6741.
[59] I. Sevilla-Noarbe, K. Bechtol, M. Carrasco Kind *et al.*, Astrophys. J. Suppl. Ser. **254**, 24 (2021).
[60] E. Huff and R. Mandelbaum, arXiv:1702.02600.
[61] E. S. Sheldon and E. M. Huff, Astrophys. J. **841**, 24 (2017).
[62] J. Zuntz, E. Sheldon *et al.*, Mon. Not. R. Astron. Soc. **481**, 1149 (2018).
[63] N. MacCrann, M. R. Becker, J. McCullough *et al.*, Mon. Not. R. Astron. Soc. **509**, 3371 (2021).
[64] E. S. Sheldon, M. R. Becker, N. MacCrann, and M. Jarvis, Astrophys. J. **902**, 138 (2020).
[65] J. Myles, A. Alarcon, and A. Amon *et al.*, Mon. Not. R. Astron. Soc. **505**, 4249 (2021).
[66] M. Gatti, G. Giannini, G. M. Bernstein *et al.*, Mon. Not. R. Astron. Soc. **510**, 1223 (2021).
[67] C. Sánchez, J. Prat, G. Zacharegkas *et al.*, Phys. Rev. D **105**, 083529 (2022).
[68] J. Muir, G. M. Bernstein, D. Huterer *et al.*, Mon. Not. R. Astron. Soc. **494**, 4454 (2020).
[69] T. M. C. Abbott, F. B. Abdalla, A. Alarcon *et al.*, Phys. Rev. D **98**, 043526 (2018).
[70] H. S. Xavier, F. B. Abdalla, and B. Joachimi, Mon. Not. R. Astron. Soc. **459**, 3693 (2016).
[71] R. Takahashi, T. Hamana, M. Shirasaki, T. Namikawa, T. Nishimichi, K. Osato, and K. Shiroyama, Astrophys. J. **850**, 24 (2017).
[72] D. Potter, J. Stadel, and R. Teyssier, Comput. Astrophys. Cosmol. **4**, 2 (2017).
[73] O. Friedrich, F. Andrade-Oliveira, H. Camacho *et al.*, Mon. Not. R. Astron. Soc. **508**, 3125 (2021).
[74] K. M. Górski, E. Hivon, A. J. Banday, B. D. Wandelt, F. K. Hansen, M. Reinecke, and M. Bartelmann, Astrophys. J. **622**, 759 (2005).
[75] V. Springel, Mon. Not. R. Astron. Soc. **364**, 1105 (2005).
[76] M. Crocce, S. Pueblas, and R. Scoccimarro, Mon. Not. R. Astron. Soc. **373**, 369 (2006).
[77] R. Takahashi, M. Sato, T. Nishimichi, A. Taruya, and M. Oguri, Astrophys. J. **761**, 152 (2012).
[78] T. Hamana, J. Sakurai, M. Koike, and L. Miller, Publ. Astron. Soc. Jpn. **67**, 34 (2015).
[79] D. Zürcher *et al.*, Mon. Not. R. Astron. Soc. **511**, 2075 (2022).
[80] F. Bernardeau, S. Colombi, E. Gaztañaga, and R. Scoccimarro, Phys. Rep. **367**, 1 (2002).
[81] R. Scoccimarro and H. M. P. Couchman, Mon. Not. R. Astron. Soc. **325**, 1312 (2001).
[82] L. Van Waerbeke, T. Hamana, R. Scoccimarro, S. Colombi, and F. Bernardeau, Mon. Not. R. Astron. Soc. **322**, 918 (2001).
[83] M. L. Brown, P. G. Castro, and A. N. Taylor, Mon. Not. R. Astron. Soc. **360**, 1262 (2005).
[84] C. Hikage, M. Takada, T. Hamana, and D. Spergel, Mon. Not. R. Astron. Soc. **412**, 65 (2011).
[85] R. Takahashi, S. Soma, M. Takada, and I. Kayo, Mon. Not. R. Astron. Soc. **444**, 3473 (2014).
[86] J. P. Cordero, I. Harrison, R. P. Rollins *et al.*, Mon. Not. R. Astron. Soc. **511**, 2170 (2022).
[87] S. Bridle and L. King, New J. Phys. **9**, 444 (2007).
[88] C. M. Hirata and U. Seljak, Phys. Rev. D **70**, 063526 (2004).
[89] S. Pyne, A. Tenneti, and B. Joachimi, arXiv:2204.10342.
[90] A. J. S. Hamilton, Mon. Not. R. Astron. Soc. **322**, 419 (2001).
[91] J. A. Blazek, N. MacCrann, M. A. Troxel, and X. Fang, Phys. Rev. D **100**, 103506 (2019).
[92] A. Porredon, M. Crocce, P. Fosalba *et al.*, Phys. Rev. D **103**, 043503 (2021).

[93] A. Porredon *et al.*, arXiv:2105.13546 [Phys. Rev. D (to be published)].
[94] N. Kaiser and G. Squires, Astrophys. J. **404**, 441 (1993).
[95] C. G. R. Wallis, J. D. McEwen, T. D. Kitching, B. Leistedt, and A. Plouviez, massmappy: Mapping dark matter on the celestial sphere, https://ui.adsabs.harvard.edu/abs/2022ascl.soft07035W.
[96] D. Gualdi, M. Manera, B. Joachimi, and O. Lahav, Mon. Not. R. Astron. Soc. **476**, 4045 (2018).
[97] A. F. Heavens, R. Jimenez, and O. Lahav, Mon. Not. R. Astron. Soc. **317**, 965 (2000).
[98] M. Tegmark, A. N. Taylor, and A. F. Heavens, Astrophys. J. **480**, 22 (1997).
[99] J. Hartlap, P. Simon, and P. Schneider, Astron. Astrophys. **464**, 399 (2007).
[100] S. Dodelson and M. D. Schneider, Phys. Rev. D **88**, 063537 (2013).
[101] O. Friedrich and T. Eifler, Mon. Not. R. Astron. Soc. **473**, 4150 (2018).
[102] W. J. Handley, M. P. Hobson, and A. N. Lasenby, Mon. Not. R. Astron. Soc. **450**, L61 (2015).
[103] W. J. Handley, M. P. Hobson, and A. N. Lasenby, Mon. Not. R. Astron. Soc. **453**, 4385 (2015).
[104] S. Habib, K. Heitmann, D. Higdon, C. Nakhleh, and B. Williams, Phys. Rev. D **76**, 083503 (2007).
[105] K. Heitmann, D. Higdon, C. Nakhleh, and S. Habib, Astrophys. J. **646**, L1 (2006).
[106] C. Doux, E. Baxter, P. Lemos *et al.*, Mon. Not. R. Astron. Soc. **503**, 2688 (2021).
[107] M. Raveri and W. Hu, Phys. Rev. D **99**, 043506 (2019).
[108] T. M. C. Abbott *et al.* (DES Collaboration), Phys. Rev. D **105**, 023520 (2022).
[109] C. Heymans, T. Tröster, M. Asgari *et al.*, Astron. Astrophys. **646**, A140 (2021).
[110] T. Hamana, M. Shirasaki, S. Miyazaki *et al.*, Publ. Astron. Soc. Jpn. **72**, 16 (2020).
[111] N. Aghanim, Y. Akrami, M. Ashdown *et al.*, Astron. Astrophys. **641**, A6 (2020).
[112] M. Raveri, G. Zacharegkas, and W. Hu, Phys. Rev. D **101**, 103527 (2020).
[113] C. Chang, M. Wang, S. Dodelson *et al.*, Mon. Not. R. Astron. Soc. **482**, 3696 (2019).
[114] M. Jarvis, E. Sheldon, J. Zuntz *et al.*, Mon. Not. R. Astron. Soc. **460**, 2245 (2016).
[115] B. Giblin, C. Heymans, M. Asgari *et al.*, Astron. Astrophys. **645**, A105 (2021).
[116] E. Krause *et al.*, arXiv:2105.13548 [Mon. Not. R. Astron. Soc. (to be published)].
[117] A. F. Heavens, E. Sellentin, D. de Mijolla, and A. Vianello, Mon. Not. R. Astron. Soc. **472**, 4244 (2017).